

5-1-2016

Seismic imaging of the lithosphere-asthenosphere boundary with a dense broadband array in central California

Charles Hoots

Follow this and additional works at: https://digitalrepository.unm.edu/eps_etds

Recommended Citation

Hoots, Charles. "Seismic imaging of the lithosphere-asthenosphere boundary with a dense broadband array in central California." (2016). https://digitalrepository.unm.edu/eps_etds/36

This Thesis is brought to you for free and open access by the Electronic Theses and Dissertations at UNM Digital Repository. It has been accepted for inclusion in Earth and Planetary Sciences ETDs by an authorized administrator of UNM Digital Repository. For more information, please contact disc@unm.edu.

Charles Hoots

Candidate

Earth and Planetary Sciences

Department

This thesis is approved, and it is acceptable in quality and form for publication:

Approved by the Thesis Committee:

Brandon Schmandt, Chairperson

Lindsay Lowe Worthington

Mousumi Roy

Seismic imaging of the lithosphere-asthenosphere boundary with a dense broadband array in central California

by

Charles Hoots

Masters of Science
Bachelors of Science

THESIS

Submitted in Partial Fulfillment of the
Requirements for the Degree of

MASTER OF SCIENCE

in Earth and Planetary Science

The University of New Mexico
Albuquerque, New Mexico

May, 2016

Acknowledgements

I would like to thank all those who helped me grow in pursuit of this body of work as a researcher and as a person. I also thank my professor, Brandon Schmandt, for his guidance and patience and the rest of my graduate committee for their support.

Seismic imaging of the lithosphere-asthenosphere boundary with a dense broadband array in central California

by

Charles Hoots

Masters of Science
Bachelors of Science

ABSTRACT OF THESIS

Lithospheric attachment to the high-velocity Isabella anomaly (IA) in central California was tested by mapping the lateral extent of interruption of the lithosphere-asthenosphere boundary (LAB). The study area spans the location of two plausible origins for the anomaly, the Monterey microplate (Wang et al., 2013) and Sierra Nevada batholith (Ducea & Saleeby, 1998). Results include 918 binned receiver functions that were made using multi-channel spectral deconvolution and an array-based spectral source estimation on the event data from an 18-month deployment of a high density array from the coast to the Sierra Nevada crossing the lateral location of the Isabella anomaly. Common conversion point (CCP) scattered wave imaging shows a strong negative velocity gradient (NVG) west of the San Andreas Fault (SAF) and a gap in a NVG horizon east of the SAF. This is interpreted as prominent arrivals at the base of a partially subducted microplate that become undetectable as the plate dips too steeply east of the SAF for reliable recovery of Sp converted phases. The gap in consistent NVG arrivals would indicate a local disruption of the LAB along the lateral extent of the anomaly. Although the LAB disruption cannot constrain the tectonic origin of the Isabella anomaly, it does indicate the anomaly is

adjacent or attached to North American lithosphere. S-to-P (Sp) conversions west of the SAF are consistent with a sharp LAB contrast, but whether the mantle section of the lithosphere is composed of Monterey microplate mantle or North America forearc mantle is unknown. Imaging also shows a weak east-dipping NVG in the eastern half of the Great Valley. This suggests a continental LAB at the western edge of the Sierra Nevada foothills down to 100km depth. Sharp changes in Sp arrivals near and shallower than the Moho are consistent with a previously imaged west dipping sub-crustal shear zone extending down to about 30 km depth beneath the Great Valley. The Moho detected 45 km below the Sierra Nevada foothills shows that at least locally there is not a Moho hole as suggested by prior studies and any interruption of the Moho at this latitude is constrained farther to the west beneath the Great Valley. The results and interpretations in this study are in agreement with prior studies (Wang et al., 2013; Pikser et al., 2012) that suggest the IA is a steeply dipping continuation of the partially subducted Monterey microplate.

Table of contents

List of Figures.....	vii
1. Introduction.....	1
2. Background.....	3
2.1 Tectonic evolution of central California.....	3
2.2 Isabella.....	5
2.3 Sp receiver functions in California.....	8
3. Hypothesis.....	8
4. Method.....	9
4.1 Receiver functions.....	9
4.2 Method summary.....	11
4.3 Data.....	12
4.4 Distance culling.....	13
4.5 Rotation.....	14
4.6 Signal-to-noise ratio (SNR) and magnitude culling.....	14
4.7 Phase culling and deconvolution windowing.....	15
4.8 Binning.....	15
4.9 Source estimation.....	16
4.10 Multi-channel deconvolution.....	17
4.11 Common conversion-point stacking (CCP) imaging.....	19
4.12 Forward modeling.....	21
5. Results.....	22
5.1 CCP imaging results.....	22
5.2 Data fold.....	23
5.3 NVG arrival amplitudes.....	25
5.4 Stacked receiver functions.....	25
5.5 Forward modeling.....	27
6. Discussion.....	28
6.1 Coastal block NVG.....	29
6.2 Absent to weak NVG in the Great Valley.....	30
6.3 Sierra Nevada foothills Moho.....	33
6.4 Deep crustal shear zone.....	33
6.5 Conclusion.....	34
References.....	36

List of Figures

- FIGURE 1.**3
Study area. Central California Seismic Experiment (CCSE) array shown in red triangles. Approximate location of the Isabella high velocity anomaly shown in blue. Bold dashed line is the San Andreas fault system. Light dashed lines are the coastal thrust block.
- FIGURE 2.**4
Summary history for the tectonic detachment of the Farallon and Pacific plate capture of the Monterey microplate over the past 28 Myr. MTJ, Mendicino triple junction; RTJ, Rivera triple junction; F, Farallon; M, Monterey; A, Arguello plate. A, Pacific ridge contact with NA forming the MTJ. B, northward propagation of dextral transform. C, Pacific-Arguello ridge makes contact with NA forming the RTJ. D, Monterey subduction is cut off and the plate assumes Pacific plate motion by 20 Ma.
- FIGURE 3.**5
(A) IA, Isabella shear velocity anomaly at 70km depth. CP, Colorado Plateau; TR, Transverse Range anomaly. Dashed line is the San Andreas Fault. Solid black line is the profile shown in B. (B) Shear velocity cross section along W-E. Isabella is shown here extending beneath the Great Valley and the western edge of the Sierras down to as much as 225km depth. Adapted from Wang et al., 2013.
- FIGURE 4.**9
A, a conceptual diagram showing the absence of a LAB in the presence of interfering lithospheric structure, the possible cause of this should be either B or C. B is the origin theory for Isabella that posits it was a delaminated piece of mafic lithosphere under the Sierra Nevada that foundered to the SSW (Zandt, 2003). C, the contending theory that proposes Isabella to be a continuation of the unsubsducted Monterey microplate under the Great Valley (Wang et al., 2013).
- FIGURE 5.**12
Teleseismic ray coverage. Red events in the map are SKS events, blue are S events. Inset Figure shows the incidence angles upon the CCSE array for all events used after culling.
- FIGURE 6.**13
Vertical component synthetic S-wave seismograms with a 10 s deg⁻¹ time reduction. The converted phases from S, SKS, and ScS waves at the Moho, LAB, 410, and 660 are marked and labelled. Blue, the area from 85-120° where SKS phases are the clear first arrivals in an S-event. Red is the area from 55-85° where direct S-waves are the clear first arrivals. Green is the area from about 80-85° where the S and SKS arrival times are similar enough to result in significant signal interference. Yellow is where direct P-wave surface reflections and the direct-P coda begin to interfere with direct-S. Adapted from Yuan et al., 2006.

FIGURE 7.	16
Source function estimate for an S-wave event. Power spectra in the P and SV direction of ground motion are shown on the blue and red traces, respectively. The P- and SV- components are offset for clarity by amplifying the SV spectra by three orders of magnitude. The black lines denote the estimated log-spectral domain of the source function as a result of stacking the spline smoothed SV-component spectra. The S-wave receiver function spectra are the result of the least-squares inversions for all bins that utilized this event.	
FIGURE 8.	19
Shear velocity model along main line of the CCSE used for ray-path migration. Model velocities are taken from Schmandt et al., 2015. V_p is defined using a constant 1.75 and 1.84 crustal and mantle V_p/V_s ratio, respectively. The model extends down to 160km.	
FIGURE 9.	20
Ray travel paths used to migrate the receiver functions into a physical volume for CCP imaging. The model used is defined in eight 3-dimensional layers for P and S velocity down to 160km. The data set consists of 295 bins, one for each ray.	
FIGURE 10.	21
P-component (S_p converted energy) synthetic seismograms for different gradients at the LAB. A, the P and S velocity model used to produce the synthetics shown in B. An LAB with a sharp (10km) change in velocity both at a high (10%) and low (5%) velocity contrast is shown in magenta and black, respectively. An LAB with a gradual (25km) change in velocity both at a high (10%) and low (5%) velocity contrast are shown in blue and red, respectively. Amplitudes near zero are negative because the source function has not been deconvolved from the synthetic seismograms.	
FIGURE 11.	22
CCP imaging results. Topographic profile on top. Receiver function amplitudes are weighted by distance within the first Fresnel zone (25km at depths for the LAB) to the ray and the number of events used to make each source-receiver pair.	
FIGURE 12.	23
The number of source-receiver pairs (logarithmic) common to each conversion point in the model. The amount of source-receiver pairs at a single point in the model ranges from 80 to 918. Triangles represent all stations in the array.	
FIGURE 13.	24
Arrival amplitudes across the array consistent with the depth and parity of the LAB. Defined as the local minima below the Moho and shallower than 110 km. The peak in the negative arrival amplitude changes abruptly at the SAF from 6-7% to 2% in the Great Valley. The dashed red line marks the lateral extent of Isabella at 70km depth. The dashed blue line is Isabella at 100km depth. Possible LAB arrivals would lie between these two outlines.	

FIGURE 14.26

Stacked receiver functions at five points of interest along the CCSE line. Solid black lines are the mean. Dashed red lines are one standard deviation from the mean after randomly resampling the mean at every depth 200 times with replacement. The blue area is the Moho, the red area is the LAB arrival heuristically defined as the first negative arrival shallower than 110km. The stacked spectra on the coast, A, have a peak LAB arrival amplitude of 6.5%. The area immediately to the west of the SAF, B, peaks at 3.4% for the LAB. The area immediately east of the SAF, C, peaks at 2.5% for the LAB. Points D and E in the western and eastern halves of the Great Valley, respectively, show no arrivals with amplitudes consistent with the expected velocity drop at the LAB. The Figure at the top is the topographic profile along the CCSE line with the point locations of A,B,C,D,E and the SAF (white line). Black line marks the lateral extent of the Isabella at depths consistent with the LAB from modern S-wave tomography (Schmandt et al., 2015). Dashed lines mark the lateral control for stacking receiver functions at each point of interest.

FIGURE 15.28

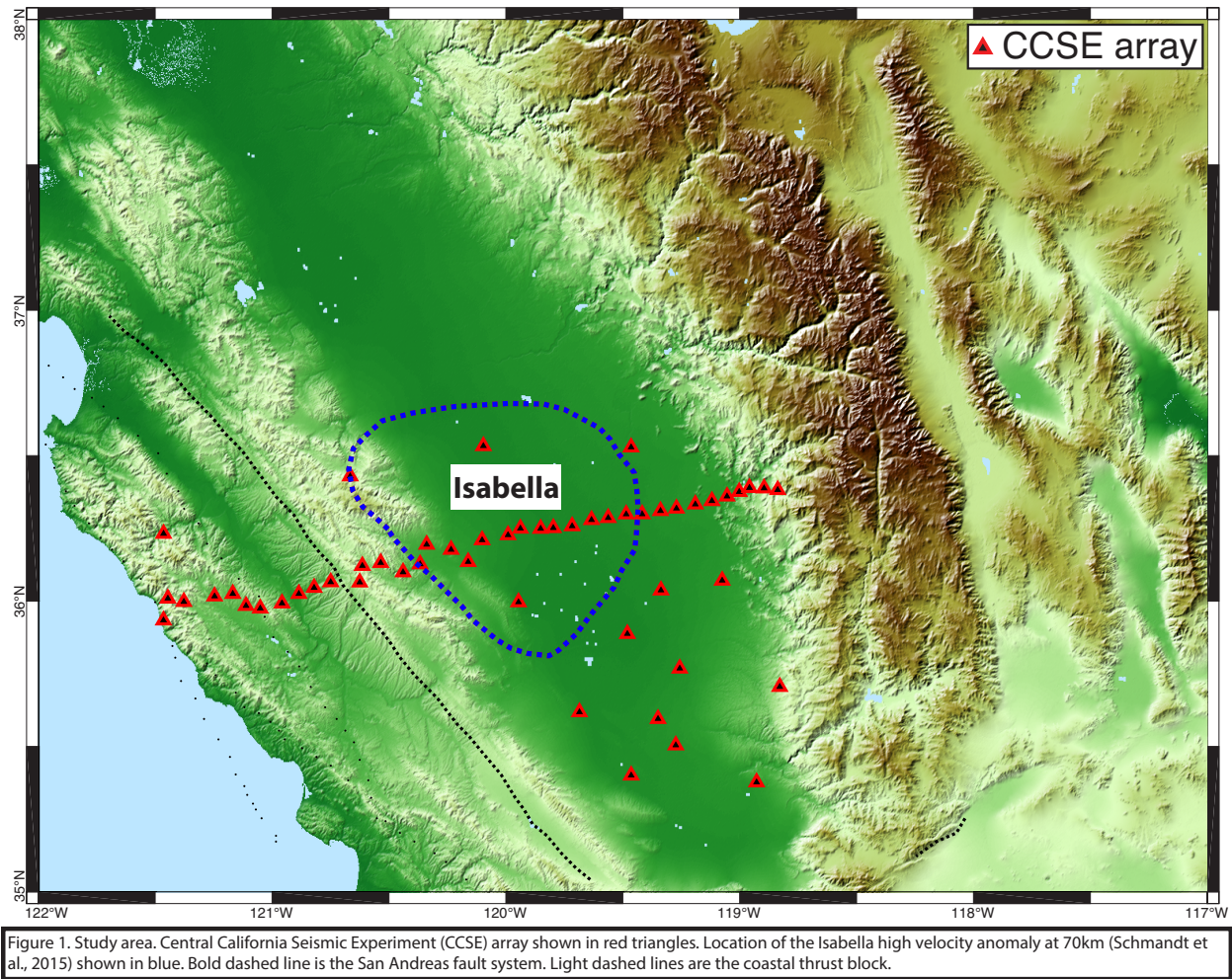
i, the preferred interpretation of CCP image. **ii**, interpretation overlaid on the shear velocity model (Schmandt et al., 2015) used in CCP imaging. Topographic profile at the top with lateral width of the Isabella at 70km implied in Schmandt et al., 2015. Orange line denotes the interpretation for the negative arrival west of the SAF as conversions at the base of partially subducted Monterey lithosphere. Dashed line denotes the approximate base of a steeply ducting Monterey lithosphere suggested in other studies (e.g. Wang et al., 2013). Green line denotes the interpreted location of a continental LAB. Blue line denotes a sharp west dipping boundary in conversions at the Moho consistent in dip and depth with a deep crustal shear zone at the base of the metamorphic belt along the Sierra foothills (Miller & Mooney, 1994). At the east end is a positive arrival ~45km in depth interpreted as conversions at a Moho beneath the Sierra Nevada, suggesting the hole observed in the Moho in other studies (e.g. Zandt et al., 2004) to be more localized to the west at these latitudes and not consistent with detachment of overlying mantle lithosphere.

1. Introduction

Over the past 45 years, significant increases in seismic network resolution have allowed the development of studies on the lithosphere and upper mantle at all scales for scattered wave (e.g. Hansen & Dueker, 2009; Levander & Miller, 2012) and tomographic (e.g. Boyd et al., 2004; Schmandt & Humphreys, 2010) imaging. The effects of these studies have married the tectonic evolution of the Earth with subsurface processes (e.g., Humphreys & Hager, 1990). Likewise, Raikes (1976) first noted a high velocity anomaly near Lake Isabella in central California, since then referred to as the 'Isabella anomaly' (IA). It was later proposed that the IA is a fragment of lithospheric delamination of the Sierra Nevada batholith that resulted in a more buoyant upper mantle and gave rise to the uplift of the southern Sierra Nevada since the Oligocene (Jones et. al, 1994). This "mantle drip" theory for the origin of Isabella was contested later with an alternative theory that the anomaly is a fragment of the Monterey oceanic lithosphere translating continuously beneath North America (Brocher et al., 1999; Wang et al., 2013). As a result of relatively sparse seismograph coverage in the Great Valley, the origin of the IA has been in contention and the topic of numerous geophysical, geochemical, and geodynamic studies (e.g. Nicholson et. al., 1992; Nicholson et. al., 1994; Ducea & Saleeby, 1998; van Wijk et. al., 2001; Zandt, 2003/2004; Saleeby & Foster, 2004; Park, 2004; Boyd et. al., 2004; Schmandt & Humphreys, 2010; Pikser et. al., 2012; Wang et. al., 2013).

This study provides constraint on the subject from the perspective of testing whether or not the IA is attached to overlying North America lithosphere by mapping seismic discontinuities in the crust and uppermost mantle using scattered wave imaging along an SW-NE profile intersecting both of the plausible origin areas of the IA. Prior studies of uppermost mantle

discontinuities in California indicate a sharp and laterally continuous discontinuity at ~50-80 km depth that is widely interpreted as the lithosphere-asthenosphere boundary (LAB; Rychert et al., 2010; Levander & Miller, 2012; Lekić & Fischer, 2013). If the IA represents actively foundering mantle lithosphere a local disruption of the sharp LAB is expected. Such a disruption has not been detected by prior studies possibly because of inadequate array resolutions for imaging a local disruption of the seismic LAB near the IA. A gap in the LAB would indicate that the IA is still attached or directly adjacent to overlying lithosphere. If there is not a gap in the sharp LAB it would indicate that the IA is detached from the overlying lithosphere and sinking through the asthenosphere. Whether or not a sharp LAB exists near the IA is evaluated with S-to-P (Sp) converted wave receiver function analysis, which isolates Sp conversions from seismic interfaces in the subsurface (Hansen & Dueker, 2009). Unlike Ps converted waves, Sp converted waves at depths of ~50 – 150 km are temporally separated from free surface S-multiples, which can interfere with imaging of the LAB (e.g. Farra & Vinnik, 2000). Sp receiver functions have been used in the past to map a continuous sharp LAB under the southwestern U.S. (Lekic et al, 2011; Ford et al., 2014; Levander & Miller, 2012). However, this study provides an order of magnitude greater station resolution near the IA because of the recently deployed Central California Seismic Experiment (CCSE) array with an average station spacing of ~7 km (Figure 1).

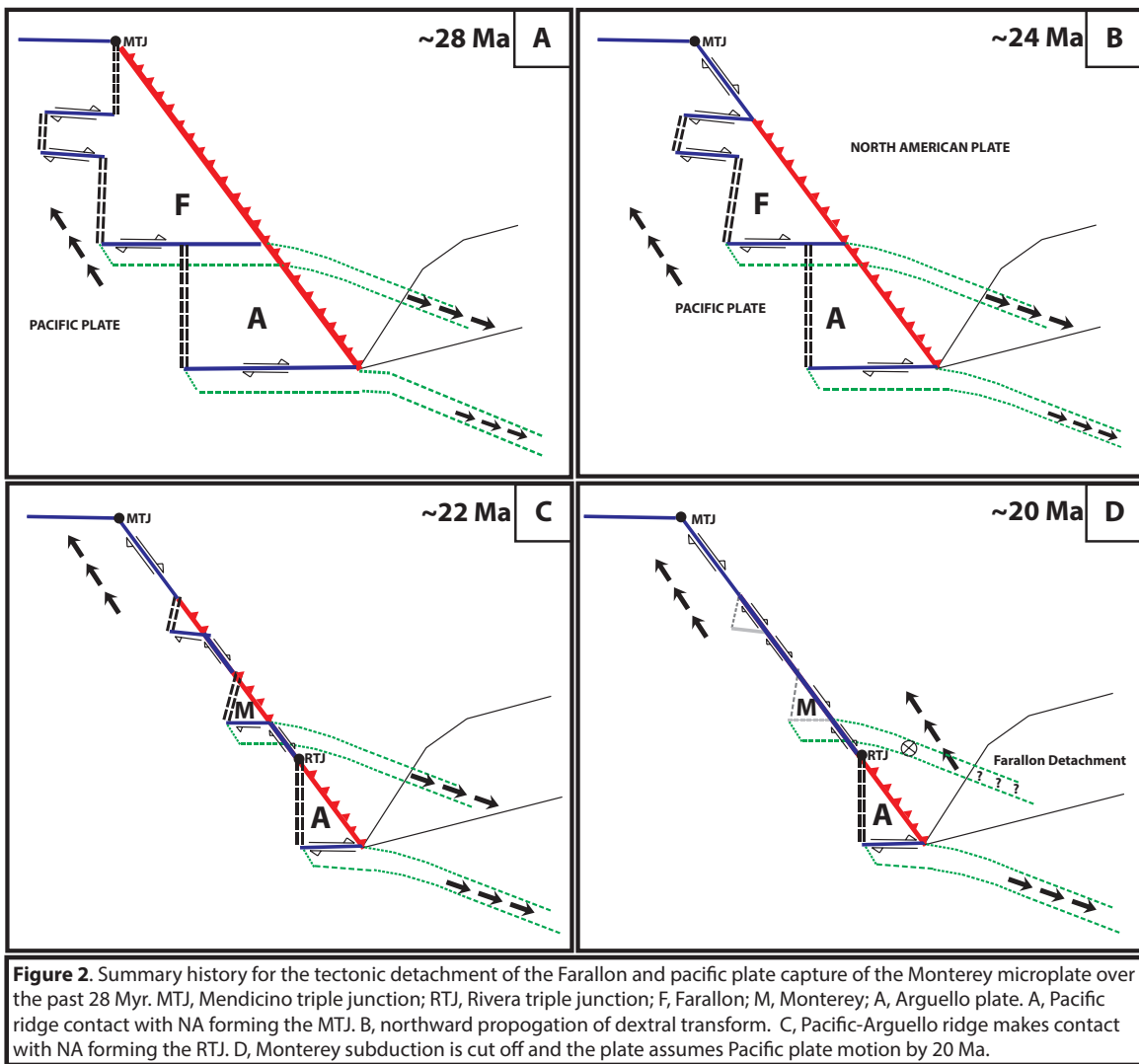


2. Background

2.1 Tectonic evolution of central California

During the Late Triassic (230 Ma), Pacific oceanic lithosphere began subduction beneath the western edge of the North American plate (Schweickert & Cowan, 1975). Long lived subduction continued up to 28 Ma when the Pacific spreading ridge encountered the western North American subduction margin near the present day latitude of $\sim 32^{\circ}\text{N}$ (Figure 2A). Two resulting triple junctions progressively shut down subduction after 28 Ma. The Mendocino triple junction has propagated north and the Rivera triple junction propagated south, with an intervening transform margin along the San Andreas fault and transtensional rift margin in the

Gulf of California (Figure 2B). By 22 Ma, the Monterey microplate was isolated on both ends by an expanding strike-slip (Lonsdale, 1991) margin (Figure 2C). Monterey-Pacific spreading ceased by 19 Ma, indicating the end of slab-pull from the subducted Farallon as a result of its detachment from the Monterey lithosphere. Farther south, Arguello-Pacific spreading continued until ~17 Ma (Figure 2D; Miller, 1992).



The two opposing triple junctions continued terminating subduction and forming right-lateral plate boundaries. This changed the margin with California from oblique northeast subduction to a transtensional dextral transform motion and the Monterey microplate was

captured by the Pacific plate (Nicholson et al., 1994). Extension of the Monterey microplate just beneath coastal California has been seismically imaged, but the eastern limit of Monterey underneath the continental lithosphere has never been fully constrained (Brocher et al., 1999; Nicholson, 1992; Meltzer & Levander, 1991). East of the Coast Ranges are the Sierra Nevada mountains, which have hosted post-subduction volcanism with mantle melts ascended through the lithosphere of the

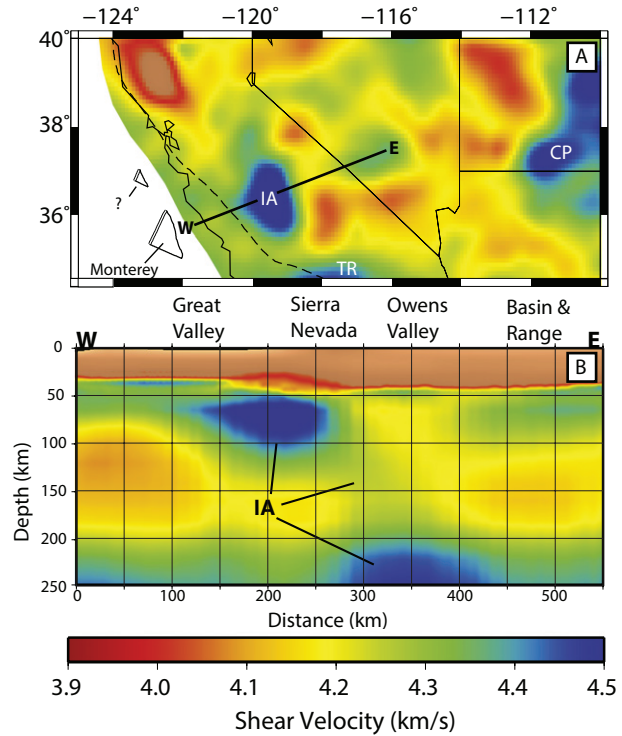


Figure 3. (A) IA, Isabella shear velocity anomaly at 70km depth. CP, Colorado Plateau; TR, Transverse Range anomaly. Dashed line is the San Andreas Fault. Solid black line is the profile shown in B. (B) Shear velocity cross section along W-E. Isabella is shown here extending beneath the Great Valley and the western edge of the Sierras down to as much as 225km depth. Adapted from Wang et. al., 2013.

primarily Cretaceous batholith (Bateman, 1967). Based upon anomalous exhumation rates of the southern Sierra Nevada and xenoliths reflecting partial melt at higher temperatures and shallower depths, prior studies hypothesize that dense eclogite-rich lower mantle lithosphere beneath the southern Sierra Nevada batholith delaminated by about 3.5 Ma (Clark, 2005; Saleeby, 2003).

2.2 The Isabella Anomaly

The IA is a high-velocity anomaly that extends in depth from ~50 to ≥ 200 km and a lateral diameter of ~100 km in recent tomography studies (Figure 3; Wang et al., 2013; Jones et al, 2014). P and S velocity structure from body and surface wave tomography of the anomaly image $\geq 3\%$ lateral velocity contrast in a near cylindrical region that dips to the east (Boyd et al., 2004; Wang

et al., 2013; Gilbert et al., 2007). Beneath the Great Valley, where the IA is inferred to be actively delaminating from the overlying lithosphere, Ps receiver functions do not identify a sharp continental Moho (Zandt et al., 2004). However, prior temporary seismic arrays have focused primarily on the Sierra Nevada and regions of California farther north and south, so there is little data to constrain the Moho and upper mantle interface structure beneath central California west of the Sierra Nevada that may be disrupted by the Isabella Anomaly.

Debate regarding the origin of the IA has persisted for over forty years, partly because the difference in predicted present day thermal profiles between a young, stalled slab and a slab window is relatively small (van Wijk et al., 2001). Two plausible origin hypotheses exist for the Isabella anomaly. One posits that it may be a continuation of the partially subducted Monterey oceanic lithosphere (Figure 4C; Wang et al., 2013). This is supported by an absence in slab-window style volcanism in the area between Isabella and the Monterey microplate (Wang et al., 2013; McLaughlin et al., 1996). If Monterey does extend as far as the IA then basal traction on the base of the continental lithosphere for 300km of Pacific plate motion could be a contributing factor to the rotation of the transverse ranges (Pikser et al., 2012; Nicholson et al., 1994). Furthermore, an influx of volatiles from a dehydrating slab at the base of the SAF could contribute to the aseismic creep, non-volcanic tremor, and ascent of mantle volatiles observed in this area (Fulton, 2009; Becken et al., 2011). Refraction and reflection surveys in the past 25 years (e.g. Meltzer & Levander, 1991; Miller et al., 1992; Henstock et al., 1997) have imaged the Monterey microplate from beneath the offshore basins to beneath California west of the San Andreas fault but cannot constrain uppermost mantle structure between the San Andreas fault and the Great Valley (Brocher et al., 1999). While the lateral extent of a basaltic layer beneath the coastal block

crust is unknown, if it were to cross the SAF, this would suggest a piece of Monterey lithosphere translating cohesively beneath North America with Pacific plate motion.

An alternative hypothesis contends that Isabella is a piece of delaminating continental lithosphere from beneath the Sierra Nevada batholith (Figure 4B; Zandt, 2003; Boyd et al, 2004). This is consistent with the timing of detachment of dense lower lithosphere from beneath the Sierra Nevada in drip models, which usually assume that the anomaly has never fully detached from the lithosphere farther west beneath the Great Valley (Saleeby et al., 2003; Le Pourhiet et al., 2006). A localized delaminating lithosphere would also be consistent with the anomalous rate of crustal subsidence centered over Isabella as well as a gravitational instability as the cause of the anomalous uplift of the Sierras after the time of detachment (Saleeby & Foster, 2004; Le Pourhiet et al., 2006). If Isabella originated from beneath the Sierra Nevada it would require SSW motion toward the plate margin relative to North America, suggesting a much more complex shallow mantle flow field (Zandt, 2003) that is inconsistent with predictions from most mantle circulation models (e.g. Silver & Holt, 2002; Becker et al., 2006). The geomorphic expression of the western Sierra changes dramatically centering over the location of the Isabella. The rivers to the north of the anomaly aggrade and drain to the North, while the rivers at and immediately to the South drain into the Tulare Lake basin, an area of anomalously high topographic subsidence overlying Isabella (Saleeby and Foster, 2004). This focused area of active subsidence overlying Isabella is consistent with a Rayleigh-Taylor convective instability (Houseman et al., 2000). While this may be used to argue the hypothesis that Isabella is delaminating lithosphere from the Sierra Nevada batholith, it does not answer the question as to why the anomalous subsidence is offset to the west of the greater Sierra batholith (Saleeby & Foster, 2004).

2.3 Sp receiver functions in California

Compared to surface and body wave travel time tomography, converted waves are more sensitive to the sharpness and contrast of sub-horizontal discontinuities (Kind et al., 2012). Unlike P waves, S waves are characterized by lower frequencies than P waves due to stronger S wave attenuation at higher frequencies in the upper mantle (Kind et al., 2012). In addition to being generally free of crustal multiples, this makes Sp receiver functions better at detecting the depth of the LAB. The largest negative Sp phase amplitude correlates well with the LAB depth inferred from surface wave tomography for the western U.S. (Abt et al., 2010; Lekic et al., 2011). Furthermore, the Sp amplitude in the tectonically active western U.S. is greater than anywhere else in the country, indicating a sharp discontinuity and large contrast in velocity across the LAB (Kind et al., 2015). If the Isabella Anomaly is still connected to the overlying lithosphere a locally broader gradient and reduced velocity contrast would be expected and consequently lower-to-negligible amplitude Sp conversions near the regional mean depth of the LAB. This difference in Sp characteristic allows for an ability to distinguish whether or not the Isabella Anomaly is still attached to the overlying North America lithosphere.

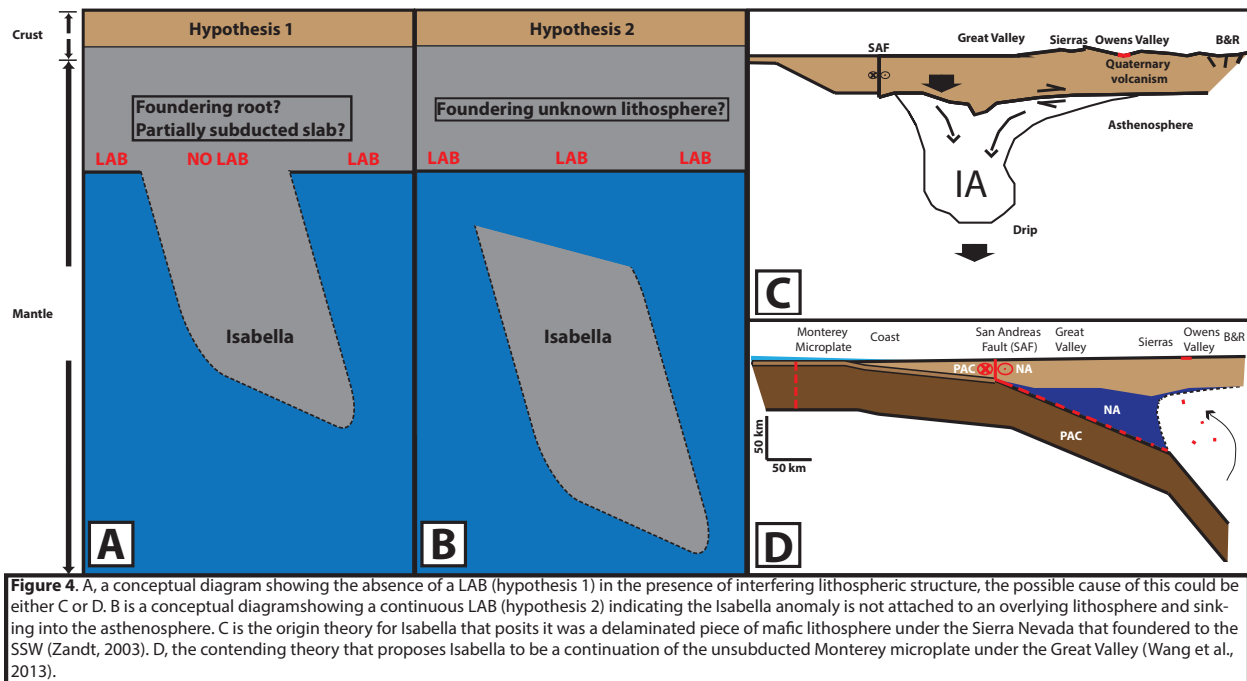
3. Hypotheses

While scattered wave imaging can not complete the argument on the origin of Isabella by itself, it is capable of providing significant constraints. The primary objective of this study is to constrain whether or not the the IA is attached to the overlying lithosphere of the Great Valley in order to test two main hypotheses:

Hypothesis 1: Negligible evidence from Sp receiver functions for a sharp LAB across the width of Isabella indicates that the anomaly is still attached to overlying Great Valley lithosphere (Figure

4A) If the position of the gap in the LAB were restricted to either the western or eastern edge of the Great Valley it would favor a fossil slab origin (Figure 4C) or Sierra Nevada root origin (Figure 4B), respectively.

Hypothesis 2: High Sp receiver function amplitudes indicative of $\geq 3\%$ Vs drop across the seismic LAB exist across the width of the Isabella Anomaly (Figure 4A), implying that the anomaly is no longer attached to the lithosphere and is sinking through the asthenosphere.



4. Method

4.1 Receiver functions

Information on the properties of the upper mantle is essential for understanding tectonic and lithospheric evolution. With knowledge on the location of major discontinuities in the upper mantle and lithosphere, inferences can be made on major structures with resolutions dependent on the data being used. To this end, receiver functions have been used for decades to look at the

crust-mantle boundary (Moho) and have more recently been employed to map discontinuities consistent with the lithosphere-asthenosphere boundary (LAB).

In 1964, Phinney proposed that the ratio of vertical (e.g. P) to horizontal (e.g. SV) energy is dependent on the structure beneath a station, which he demonstrates by identifying the base of the Moho discontinuity. Burdick and Langston (1977) performed a similar technique in the time-domain by comparing the amplitude, and later timing (Langston, 1979), of an incident P wave on the Moho to the resulting scattered phases (Ps). More recently, a technique to identify the conversion of S-to-P at upper mantle discontinuities (Farra & Vinnik, 2000) has been applied to mapping the LAB (e.g. Vinnik et al., 2005; Li et al., 2007; Savage & Silver, 2008; Hansen et al., 2009; Rychert et al., 2010). Receiver functions have also been in many other studies of mantle discontinuities, including identifying depth of the Moho (e.g., Zhu & Kanamori, 2000; Yan & Clayton, 2007b), the dip of the Moho (e.g., Yan and Clayton, 2007a), and mantle transition zones at 410 km and 660 km (e.g., Gurrola et al., 1994).

The advantage of using receiver functions to find discontinuities is the sensitivity to sudden changes in material velocity in the vertical direction. This is superior to other methods used in imaging the LAB such as surface wave tomography which can not distinguish velocity changes in the mantle that occur instantaneously from those spread over many kilometers (Eaton et al., 2009) or body-wave tomography which lacks vertical resolution in the uppermost mantle as most waves comes in at near-vertical incidence. Both P- (Rychert et al., 2005; Chen et al., 2009) and S-wave receiver functions have been used to observe the LAB but strong crustal reverberations from incident P- and Ps-waves generally limits detection of the LAB to S-receiver functions.

Similar to body-wave tomography, the seismic information employed in receiver functions is also mostly vertical however unlike body-waves the depth information is not integrated with the receiver function and thus relies on an independent velocity model to migrate the receiver functions to the depth domain. The viability of receiver function detection of the LAB is best using mostly vertically incident waves, at no more than 40° , from teleseismic waves between distances $55-85^\circ$ for S and $\geq 85^\circ$ for SKS (Yuan et al., 2006). Utilizing nearly vertical incidence angles on discontinuities beneath stations ensures higher lateral resolution as opposed to techniques similar to wide-angle reflection and refraction which tend to have more than 100 km of lateral movement through the crust and upper mantle depending on the phases used (e.g. PmP, Pn; Zhu and Kanamori, 2000).

4.2 Method summary

Teleseismic receiver functions are Green's function for teleseismic body wave sources with angles of incidence less than ~ 40 degrees. They are empirically defined through the separation of a teleseismic event source signal from the local Green's function by deconvolution. The process of scattered wave imaging using receiver functions in this experiment begins with the rotation and culling of teleseismic event data (Vinnik, 1977) followed by a spectral estimation of the source signal and deconvolution of the source signal estimate from the observed seismograms using a multi-channel inversion method (Hansen and Dueker, 2009). The resulting receiver functions are then used to create a 3-D structural image using common-conversion point (CCP) stacking (Dueker and Sheehan, 1998). Forward modeling is then performed to evaluate the plausible range of amplitudes and sharpness of structural interfaces identified in the CCP image.

4.3 Data

The most basic goal when processing seismic data for receiver functions is to isolate the weak scattered (converted) signals that are created at a discontinuity such as the LAB. No matter the technique used, the quantity and quality of the event data is essential to this goal. The ray path distance travelled for S and SKS phases range from 6,000 to 19,000 km from source to receiver, encountering all ray path phenomena that leads to scattering and attenuation before it arrives at the LAB beneath the station. From what energy remains at this point, only a very small percentage of it on the order of $\leq 1-10\%$ is converted at the discontinuity to an Sp phase, the signal sought in this experiment. Multiple techniques (sections 4.4-4.8) are used to improve the resolution of this signal for receiver function processing.

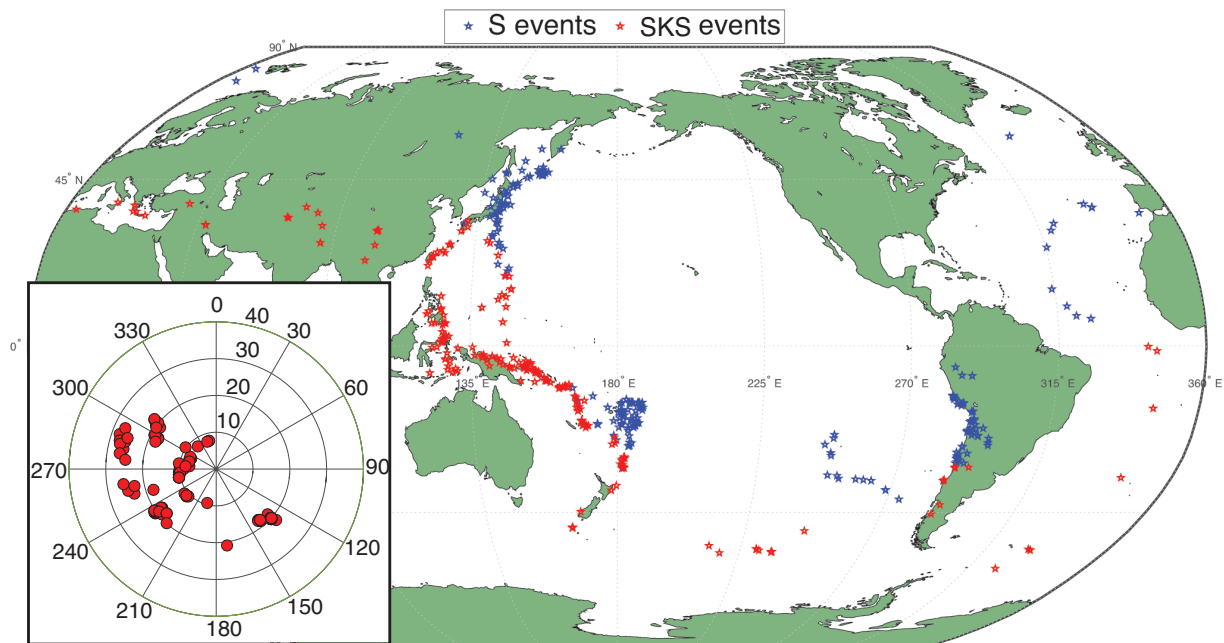


Figure 5. Teleseismic ray coverage. Red events in the map are SKS events, blue are S events. Inset Figure shows the incidence angles upon the CCSE array for all events used after culling.

This experiment utilizes the complete dataset for the CCSE array, which includes an 18 month continuous deployment of 38 three-component broadband stations along a E-W profile

line with an average spacing of ~ 7 km from the coastline to the Sierra Nevada with 15 outliers (7 of which were deployed for only 5 months) located 25-60 km from the main line (Figure 2). Similar station spacing in other settings has been sufficient to image young subducting oceanic lithosphere (e.g., Rondenay et al., 2001). All stations used broadband seismometers including Guralp 30T and Nanometrics Trillium three-component velocity sensors.

4.4 Distance culling

While Sp conversions at depths consistent with the LAB are usually deeper than most P-wave multiples, such surface reflections (e.g. PP, PPP, etc.) may arrive with significant amplitudes prior to S, still causing interference with Sp conversion amplitudes at the LAB (Yuan et al., 2006). This may result in the weaker conversions being masked (Bock, 1994) which is generally avoided with culling of teleseismic distances, however low-velocity sedimentary layers such as the Great

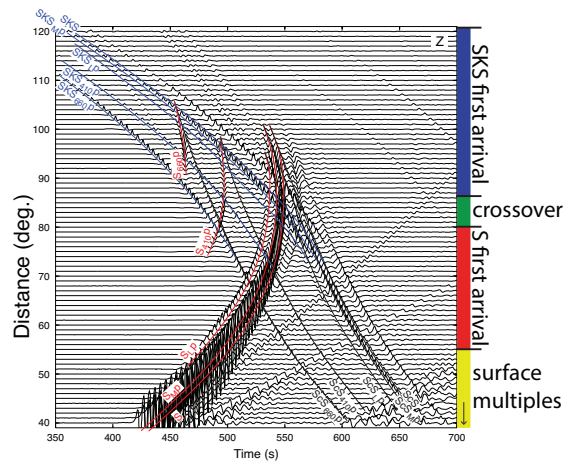


Figure 6. Vertical component synthetic S-wave seismograms with a 10 s deg⁻¹ time reduction. The converted phases from S, SKS, and ScS waves at the Moho, LAB, 410, and 660 are marked and labelled. Blue, the area from 85-120° where SKS phases are the clear first arrivals in an S-event. Red is the area from 55-85° where direct S-waves are the clear first arrivals. Green is the area from about 80-85° where the S and SKS arrival times are similar enough to result in significant signal interference. Yellow is where direct P-wave surface reflections and the direct-P coda begin to interfere with direct-S. Adapted from Yuan et al., 2006.

Valley that trap seismic noise can still cause interference. Furthermore, a crossover in arrival times for S and SKS exists around 80-85° and beyond 120° SKS phase often has low signal-to-noise ratio (Kennet and Engdahl, 1991; Astiz et al., 1996). For these reasons, event distances of 55-85° for S and 85-120° for SKS are used (Figure 5; Wilson, 2006; Yuan et al., 2006). The minimum and maximum event distance for S insulates the converted phase from the P coda and ensures plane wave arrival across the array and lies outside the critical incidence for S and lies outside the S/SKS

crossover (Yuan et al., 2006; Figure 6). The minimum and maximum event distance for SKS avoids the S/SKS crossover and interferences with P phases, respectively (Figure 6).

4.5 Rotation

Optimized rotation of the components of ground motion is important for identifying and enhancing the weak converted signals (Kind et al., 2012). Since the incident S and SKS used are vertically polarized shear waves (SV) and the converted daughter phase, Sp, is a vertically polarized compression wave, rotation of the raw seismic trace from the Z-N-E reference system to P-SV-SH will isolate the parent phase and converted phase on separate components. Using back azimuth to the event (ba) and a ray parameter based on a reference model (Ak135c), the arriving incidence angle (i) is found and used in the rotation matrix to P-SV-SH (Ferguson, 2009; eq. 1). Over or under estimation of the incidence angle can result in loss of converted phase energy to the SV component.

$$\begin{bmatrix} P \\ SV \\ SH \end{bmatrix} = M_{3D} \begin{bmatrix} Z \\ E \\ N \end{bmatrix}; \quad M_{3D} = \begin{bmatrix} \cos i & -\sin i \sin ba & -\sin i \cos ba \\ \sin i & \cos i \sin ba & \cos i \cos ba \\ 0 & -\cos ba & \sin ba \end{bmatrix} \quad (eq.1)$$

4.6 Signal-to-noise ratio (SNR) and magnitude culling

The amplitude ratio between P and S waves depends on numerous factors, for example, orientation and frequency content of the source. In the case between S and its daughter phase Sp, source side effects are removed with receiver function processing and the amplitude ratio is now primarily a function of the velocity contrast and thickness of the discontinuity, the incidence angle upon the discontinuity, the attenuation between the discontinuity and the receiver, and contaminating phase energy (e.g. PP, PPP). The cumulative effect of all these factors can lead to less than ideal receiver functions. For this reason, a user defined short-time-average (STA) to

long-time-average (LTA) ratio of 1.7 for S and 1.9 for SKS was used as the minimum threshold before utilizing the event and for only those seismic events $M_b \geq 5.5$, with the STA window duration of 3 sec. and LTA window duration of 24 sec. A higher minimum STA/LTA was used for SKS because there is a higher risk of contamination by the S-wave coda at and for a few degrees beyond the crossover distance ($\sim 80-88^\circ$).

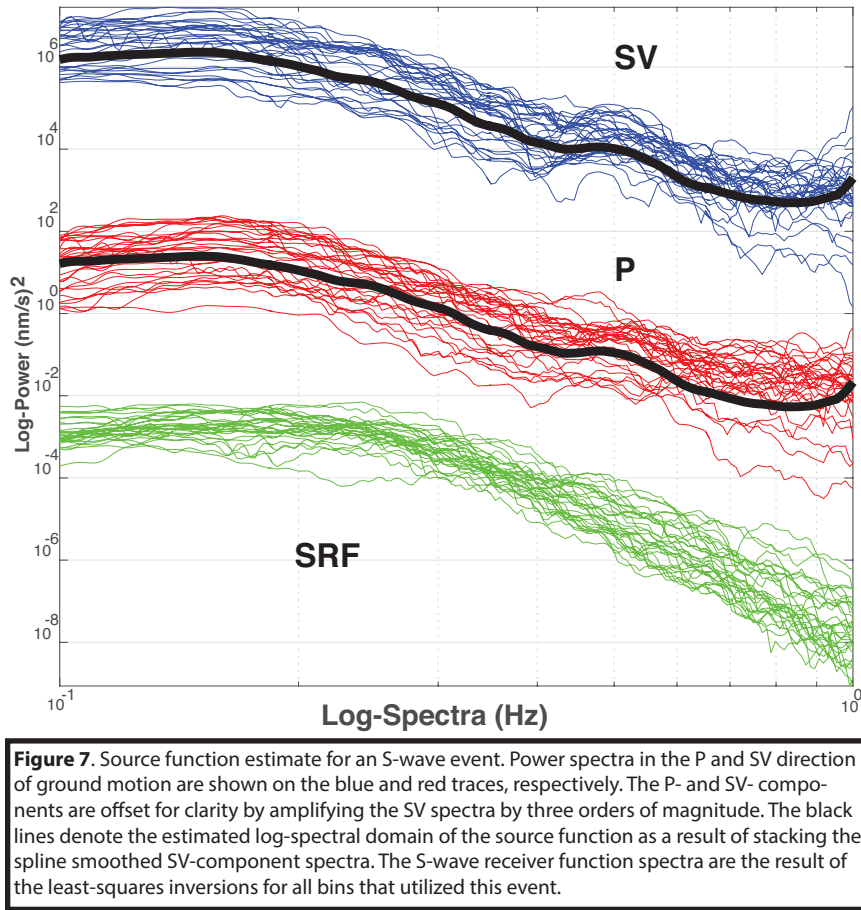
4.7 Phase culling and deconvolution windowing

Once the event has passed all prior mentioned criteria, the multi-channel cross-correlation method of Vandecar and Crosson (1990) is used to calculate travel time residuals. This is performed by isolating the trace signal of parent (S,SKS) and converted phase energy (S_p) through visually windowing and aligning by multi-channel waveform cross-correlation. Using the aligned SV waveforms the deconvolution window is defined as the 100s including and prior to the direct S/SKS arrival. For receiver functions that follow the same amplitude convention as P_s , the parity of the trace is then flipped prior to deconvolution. Unlike P_s , the initial impulse, direct S/SKS, arrives at the receiver after the converted phase but to maintain a near minimum phase assumption (4.10) for the receiver function spectra, the impulse must occur at the start of the trace followed by lower amplitude arrivals such as the S_p phase. For this reason, the trace is also reversed in time prior to deconvolution.

4.8 Binning

To ensure all events used for a single receiver function encountered the same transmission path phenomena from a similar source location to receiver, event data was then placed in non-overlapping bins defined by slowness (with incidence angles $\leq 40^\circ$) and back-azimuth. This resulted in one receiver function for each bin and one source function for each

event for the entire array that observed the event (Bostock, 2004; Baig et al., 2005; Mercier et al., 2006).



4.9 Source estimation

An initial source estimation is required for the deconvolution to have an over-determined system yielding a unique and reproducible receiver function. Since (2) is the convolution of a continuous band-limited source with an impulsive Green's function in the time domain, then the log-spectral domain (3) is the superposition of a smoothed band-limited source, assuming minimal source-side scattering, with a rough and statistically white Green's function spectra (Escalante et al., 2007). Under this assumption, the source function log-spectra can be estimated using spectral smoothing (Claerbout, 1992). This is applied by fitting a piecewise continuous cubic

spline function to the observed spectrum that optimizes the trade-off between data fit and smoothness for each station observing the event and then linearly stacked (**Figure 7**).

4.10 Multi-channel deconvolution

A teleseismic wave observed at a station consists of the original source function for the event convolved with the Earth's response to that source function which includes converted phases from reverberations caused by near surface structure such as the LAB. Obtaining a receiver function for a station focuses on deconvolving these two pieces of information from the observed signal (Langston, 1979).

Consider an event, \mathbf{m} , observed at a station such that

$$\mathbf{P}_m(t) = S_m(t) * \mathbf{G}(t) \quad (2).$$

Where the seismic trace, $\mathbf{P}_m(t)$, is expressed as the convolution of the source function, $S_m(t)$, and the Earth 3-component response function to the source, $\mathbf{G}(t)$. Transforming (1) into the log-spectral domain linearizes the equation such that

$$\text{Log}\{|\mathbf{P}_m(\omega)|\} = \log \{|S_m(\omega)|\} \mathbf{I}_3 + \log \{|\mathbf{G}(\omega)|\} \quad (3).$$

Where the source and Green's function are defined as

$$\mathbf{P}_m(\omega) = [P_m(\omega), SV_m(\omega), SH_m(\omega)]^T \quad (4) \text{ and}$$

$$\mathbf{G}(\omega) = [G^P(\omega), G^{SV}(\omega), G^{SH}(\omega)]^T \quad (5), \text{ respectively.}$$

Note that all \mathbf{m} events are organized such that they have similar back-azimuth and slowness to ensure that that each event in the deconvolution encounters the same ray-path phenomena. This

allows the receiver function, \mathbf{G} , to be the same for each event. Expanding (2) into a system of equations for \mathbf{m} events and augmenting with \mathbf{m} source function estimates, $\hat{S}_m(\omega)$, yields

$$\begin{bmatrix} I_3 & 1 & \cdots & 0 \\ 0 & 1 & \cdots & 0 \\ \vdots & \vdots & \ddots & \vdots \\ I_3 & 0 & \cdots & 1 \\ 0 & 0 & \cdots & 1 \end{bmatrix} \begin{bmatrix} \log\{G(\omega)\} \\ \log\{|S_1(\omega)|\} \\ \vdots \\ \log\{|S_m(\omega)|\} \end{bmatrix} = \begin{bmatrix} \log\{P_1(\omega)\} \\ \log\{|\tilde{S}_1(\omega)|\} \\ \vdots \\ \log\{|\tilde{S}_m(\omega)|\} \\ \log\{P_m(\omega)\} \end{bmatrix} \quad (5)$$

The solution to (5) results is a log amplitude spectral estimate of the 3-component Green's function. We can then assume the SV component trace to be minimum phase as the trace used in the deconvolution includes the direct arrival (e.g. S, SKS) and 100 seconds prior to the direct arrival of lower amplitude scattered waves, making the trace near minimum phase. Under this minimum phase assumption, the phase spectra can be reconstructed by applying several all-pass filters to the amplitude spectra which then can be used to transform the three-component Green's function to the time domain (Bostock, 2004). This entire deconvolution procedure is then repeated for individual stations in each bin of events that are defined by overlapping slowness and back-azimuth.

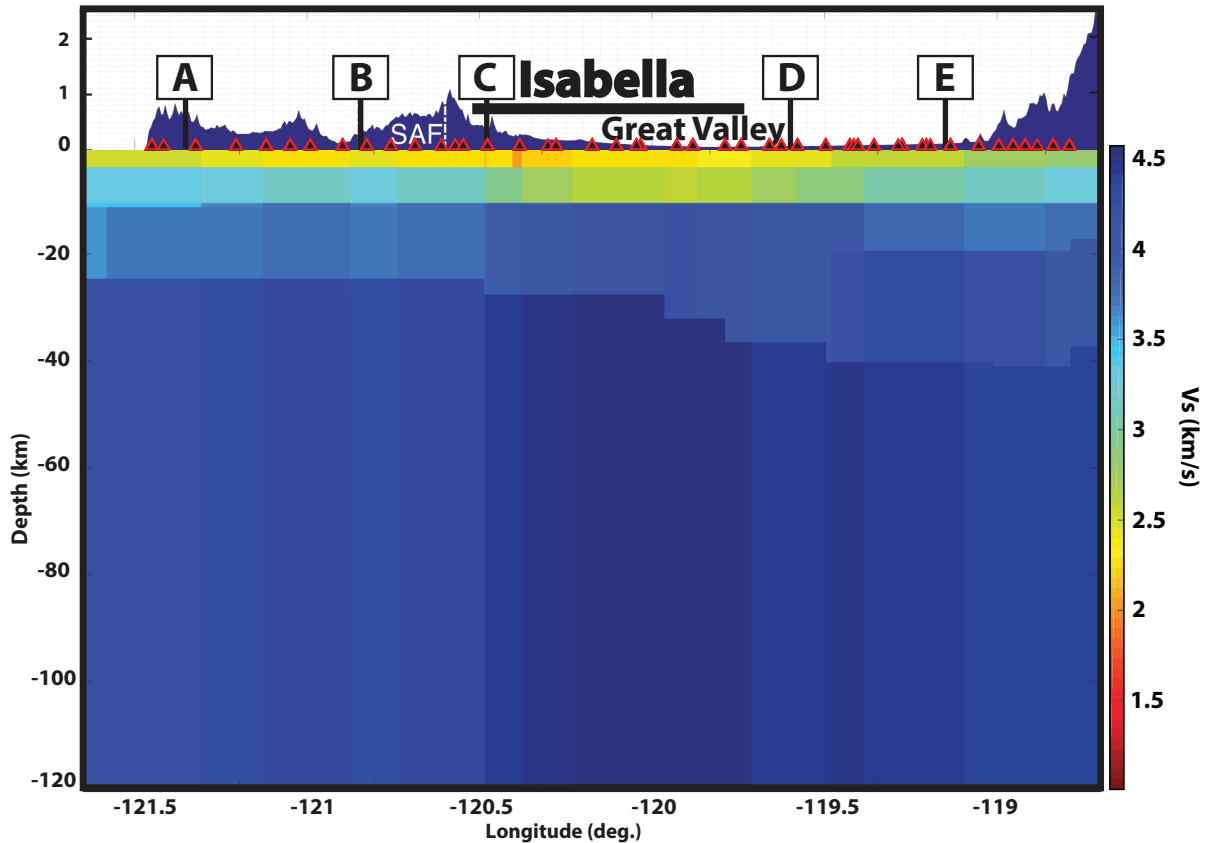


FIGURE 8. Shear velocity model along main line of the CCSE used for ray-path migration. Model velocities are taken from Schmandt et al., 2015. V_p is defined using a constant 1.75 and 1.84 crustal and mantle V_p/V_s ratio, respectively. The model extends down to 160km.

4.11 Common conversion-point stacking (CCP) imaging

The method of common conversion-point (CCP) stacking relies on the idea that rays intersecting in the sub-surface at a discontinuity should have similar converted phase amplitudes and thus by stacking the amplitudes at these piercing-points the signal can become more resolved (Dueker & Sheehan, 1998). To create a CCP image, the receiver function amplitudes are

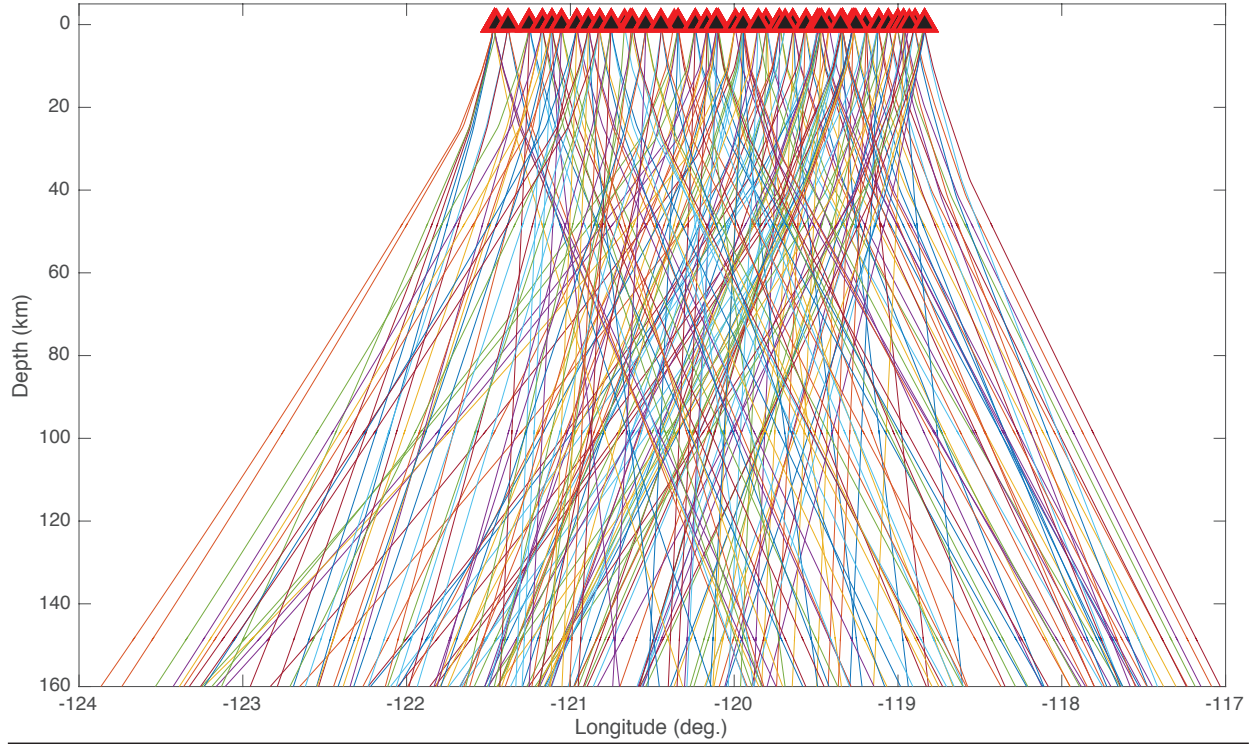


Figure 9. Ray travel paths used to migrate the receiver functions into a physical volume for CCP imaging. The model used is defined in eight 3-dimensional layers for P and S velocity down to 160km. The data set consists of 295 bins, one for each ray.

migrated into a physical 2D volume defined by depth, latitude, and longitude using 1D ray tracing along the bin back-azimuth and ray parameter for each station using the velocity model of Schmandt et al. 2015 GRL (Figure 8). The model slice beneath the line is defined every 1km in depth and 0.03° along profile (~ 3.3 km). The amount of contribution every receiver function gives to each point in the model is defined as a function of the model point distance relative to Fresnel zone width for the dominant period in each receiver function projected into the model space around the ray path also mapped into the model space (Figure 9).

Let Δ_h be the horizontal distance between a point in the model and a given receiver function at the same depth. The Fresnel zone half width, Δ^0 , for the receiver function with a dominant wavelength of λ at depth z_k is defined as

$$\Delta^0(\lambda) = \sqrt{\left(\frac{\lambda}{4} + z_k\right)^2 - z_k^2} \quad (6).$$

The weighted average contribution a receiver function gives to each point at z_k in the slice is then defined as

$$\gamma(\Delta_h) = e^{\left(\frac{\Delta_h}{\Delta^0}\right)^2} \quad (7).$$

This yields a slice of subsurface velocity gradients along the array line (section 5).

4.12 Forward modeling overview

At this phase of the experiment interpretation of the resulting scattered wave image will be required. Simple 1D synthetic seismograms are made to measure theoretical Sp conversion amplitudes across varying hypothetical scenarios for the LAB, or lack thereof (Figure 10). The 1D approach uses the reflectivity method of Fuchs and Mueller (1971). As there is much lateral heterogeneity from the coast to the Sierras in

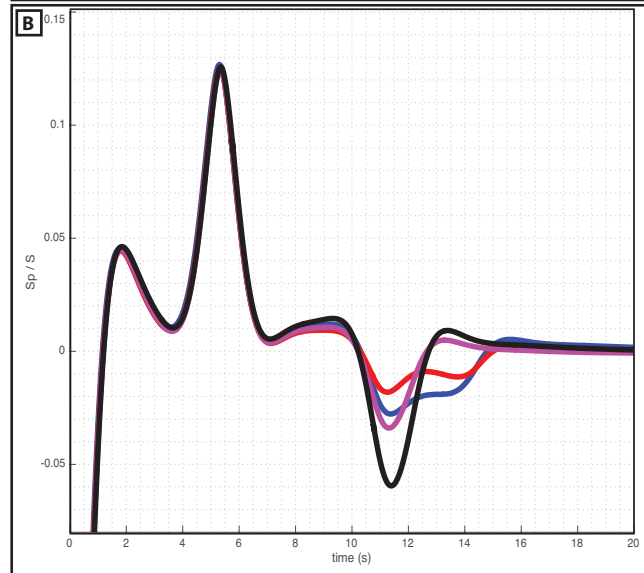
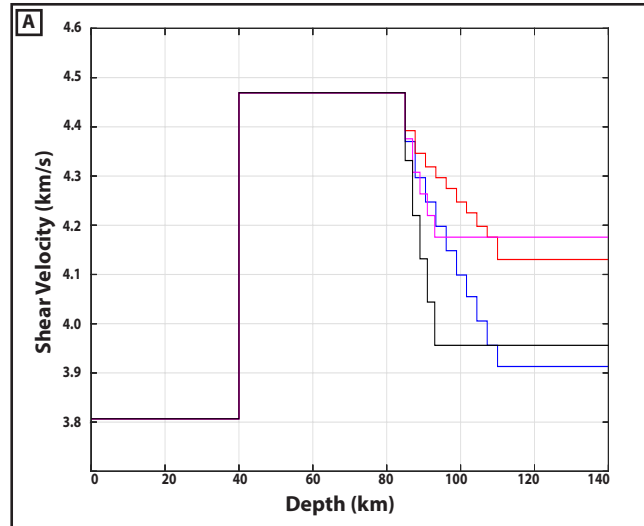


Figure 10. P-component (S_p converted energy) synthetic seismograms for different gradients at the LAB. A, the P and S velocity model used to produce the synthetics shown in B. An LAB with a sharp (10km) change in velocity both at a high (10%) and low (5%) velocity contrast is shown in magenta and black, respectively. An LAB with a gradual (25km) change in velocity both at a high (10%) and low (5%) velocity contrast are shown in blue and red, respectively. Amplitudes near zero are negative because the source function has not been deconvolved from the synthetic seismograms.

terms of tectonic regime and geologic development, multiple scenarios are tested. From all previous studies of the LAB in the region the range of values for S_p conversion amplitudes are consistent with arrivals across sharp and broad gradients from 10 to 25-km with 5-10% shear velocity contrasts (Figure 10). If the LAB arrival is weak near the Isabella Anomaly, the key goal of forward modeling will be to determine the minimum gradient thickness and maximum shear

velocity contrast that would result in an arrival amplitude consistent with those observed in the CCP imaging.

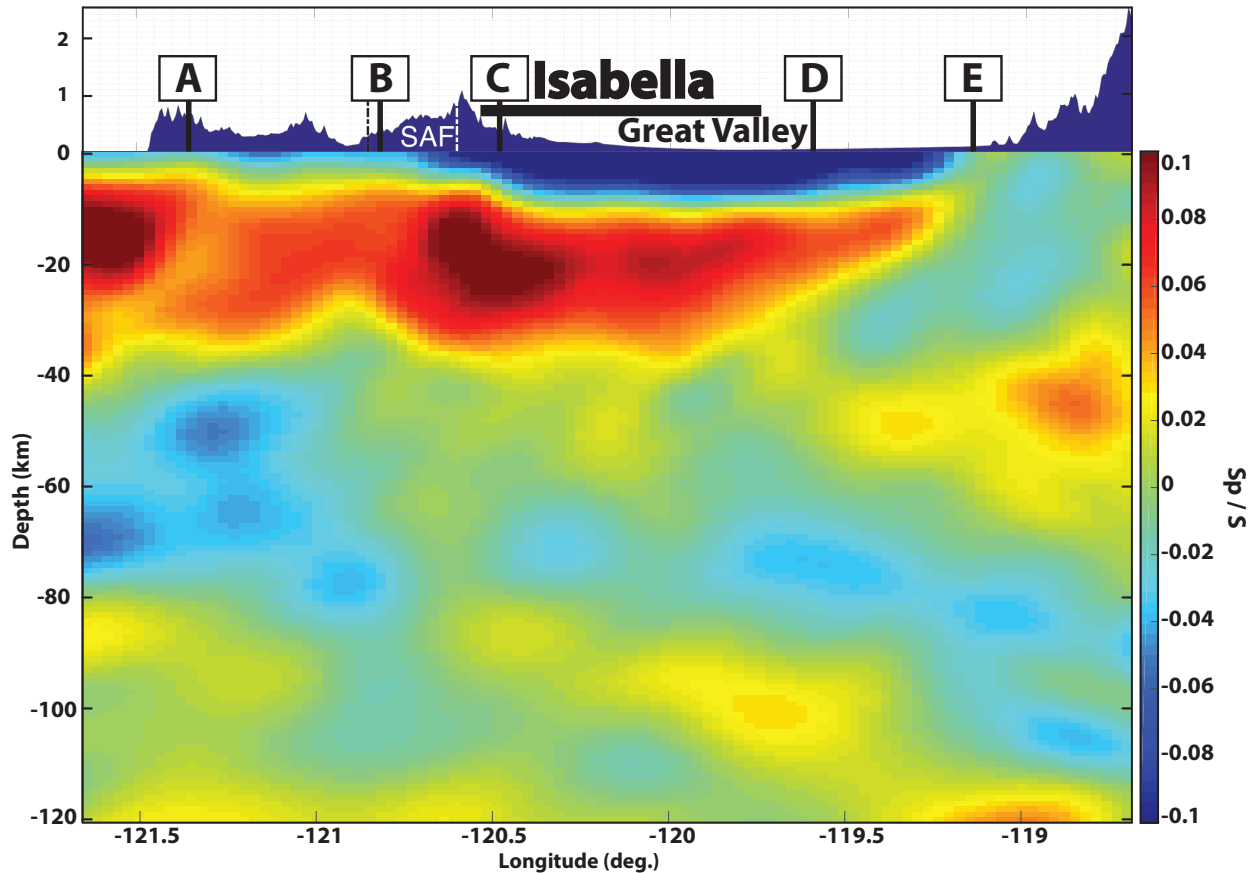


Figure 11. CCP imaging results. Topographic profile on top. Receiver function amplitudes are weighted by distance within the first Fresnel zone (25km at depths for the LAB) to the ray and the number of events used to make each source-receiver pair.

5. Results

5.1 CCP imaging results

Figure 11 shows a CCP image across the main line of the CCSE (Figure 2 & 13) from the coast to the Sierras using 918 binned receiver functions. West of the SAF exist a large area of localized negative velocity gradients (NVG) from 45-85 km. The 10-15km wide negative arrivals consistently show conversions at 6% of direct-S nearest to the coast line (-121.5°), by -121° they have diminished to ~3.5%. Across the Great Valley from -120.45° to -119° at depths 70-100km, NVG amplitudes are greater than 2.5% in only isolated sections. The locations of the greatest

NVG amplitude are located along a coherent dipping horizon beneath the eastern half of the Great Valley, but at most only <3% of direct-S. Beginning beneath the Sierra Nevada and dipping West to the middle of the Great Valley, exists a sharply defined change from prominent positive arrivals consistent in depth with the Moho to diminished to absent arrivals for Ps conversions. Positive arrivals appear again at a deeper and more localized depth at the eastern end of the image at 45km depth at the eastern edge of the image.

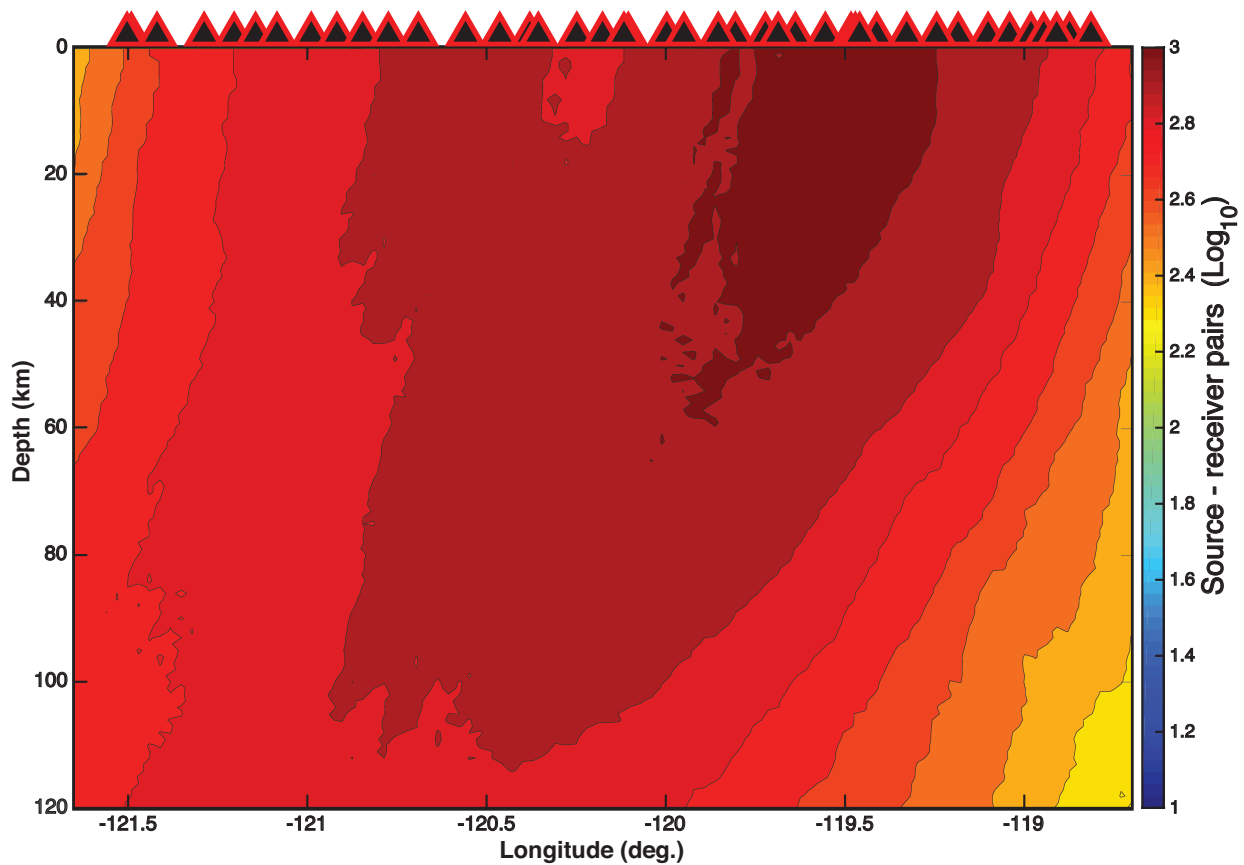


Figure 12. The number of source-receiver pairs (logarithmic) common to each conversion point in the model. The amount of source-receiver pairs at a single point in the model ranges from 80 to 918. Triangles represent all stations in the array.

5.2 Data fold

The CCSE array recorded continuously over an 18 month deployment resulting in 97 quality events for a total of 3,912 seismic traces (average 41 stations per event) used to make 918 binned receiver functions. Each bin has an average of 4.4 source-receiver pairs. Hereafter in the text

binned receiver functions are referred to as receiver functions. Figure 12 shows the number of receiver functions stacked at every point in the model systematically increasing toward the center of the array beneath the Great Valley. The peak in data fold is the approximate lateral location of the diminished <3% NVG arrivals observed in Figure 12. This is important as low signal-to-noise S waveforms are common in the valley making it an area of the model that requires the greatest amount of stacking to achieve quality results. The edges of the model are the lowest but still well over 100 receiver functions. The west dipping trend of the data fold alludes to the fact that the bulk source of the events used in this experiment came from the western Pacific.

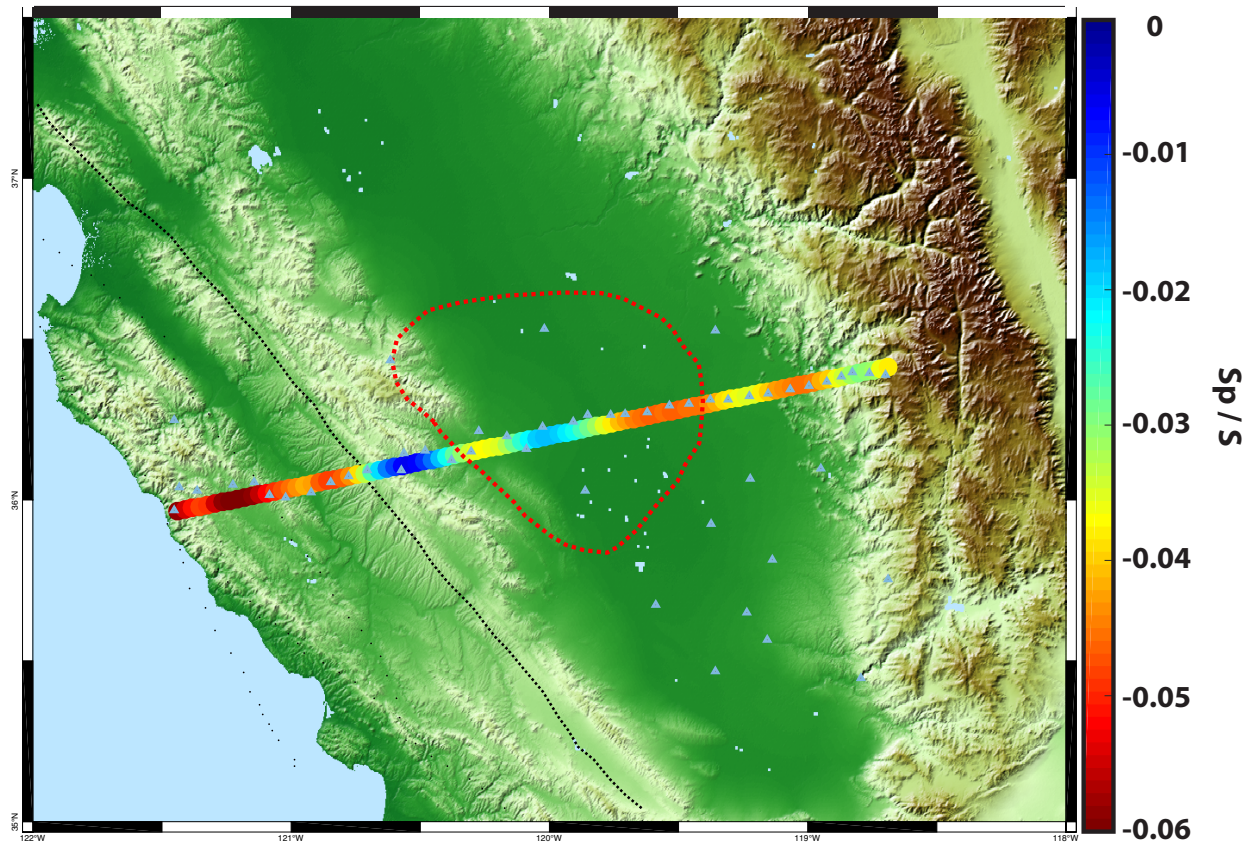


Figure 13. Arrival amplitudes across the array consistent with the depth and parity of the LAB. Defined as the local minima below the Moho and shallower than 110 km. The peak in the negative arrival amplitude changes abruptly at the SAF from 6-7% to 2% in the Great Valley. The dashed red line marks the lateral extent of Isabella at 70km depth from shear velocity model by Schmandt et al., 2015. LAB arrivals would be expected to arrive around this depth.

5.3 NVG arrival amplitudes

Figure 13 puts the NVG amplitudes into context with the rest of the major fault systems in California as well as the lateral outline of Isabella at 70km(red) and 100km(blue). NVG arrival amplitudes change dramatically when crossing the SAF. Within 25km of the SAF, the amplitudes drop below 4%. The smaller conversions in the Great Valley occur at the lateral locations (and depths) of the IA within its 100 and 70km outlines from Wang et al., 2012.

5.4 Stacked receiver functions

Five traces made by stacking all receiver functions across distinct areas of interest are shown in Figure 14. The power spectra across all receiver functions peaks and begins to taper off by about 0.24 Hz (Figure 15), indicating a dominant period of ~4 sec across each receiver function or about 25km dominant wavelength at depths consistent with the LAB. Since the minimum resolvable length scale is $\lambda/4$ (Sheriff & Geldart, 1995), layer thicknesses larger than 6.25km are resolvable. This is primarily controlled by the frequency content of the source mechanism and the bandpass filter from 3-30s period applied to the receiver functions. The receiver functions in each stack were randomly resampled with replacement 200 times to find one standard deviation of the mean, which is a measure of the stability of the mean amplitude at each depth in the stacks. 1-sigma standard deviation of the resampled mean varies by 15-28% of the peak NVG amplitude across the array. The amount of change in this variation across the array diminishes in proportion to source-receiver pairs, peaking at a 1-sigma deviation of 0.9%. NVG amplitudes greater than 1-sigma of the randomly resampled mean are evaluated and compared with synthetic receiver functions in the next section (5.5).

The receiver function stack at **A** on the coast have a mean NVG amplitude of $6.0\% \pm 0.7$. The receiver functions at **B** just west of the SAF have a mean peak NVG arrival amplitude of $3.7\% \pm 0.7$. The receiver functions at **C** just east of the SAF have a mean peak NVG amplitude of $2.8\% \pm 0.9$. Points **D** and **E** in the Great Valley have very small negative arrival amplitudes $<0.9-3.0\% \pm 0.7$. **D** goes through the points of highest NVG amplitudes in the Great Valley.

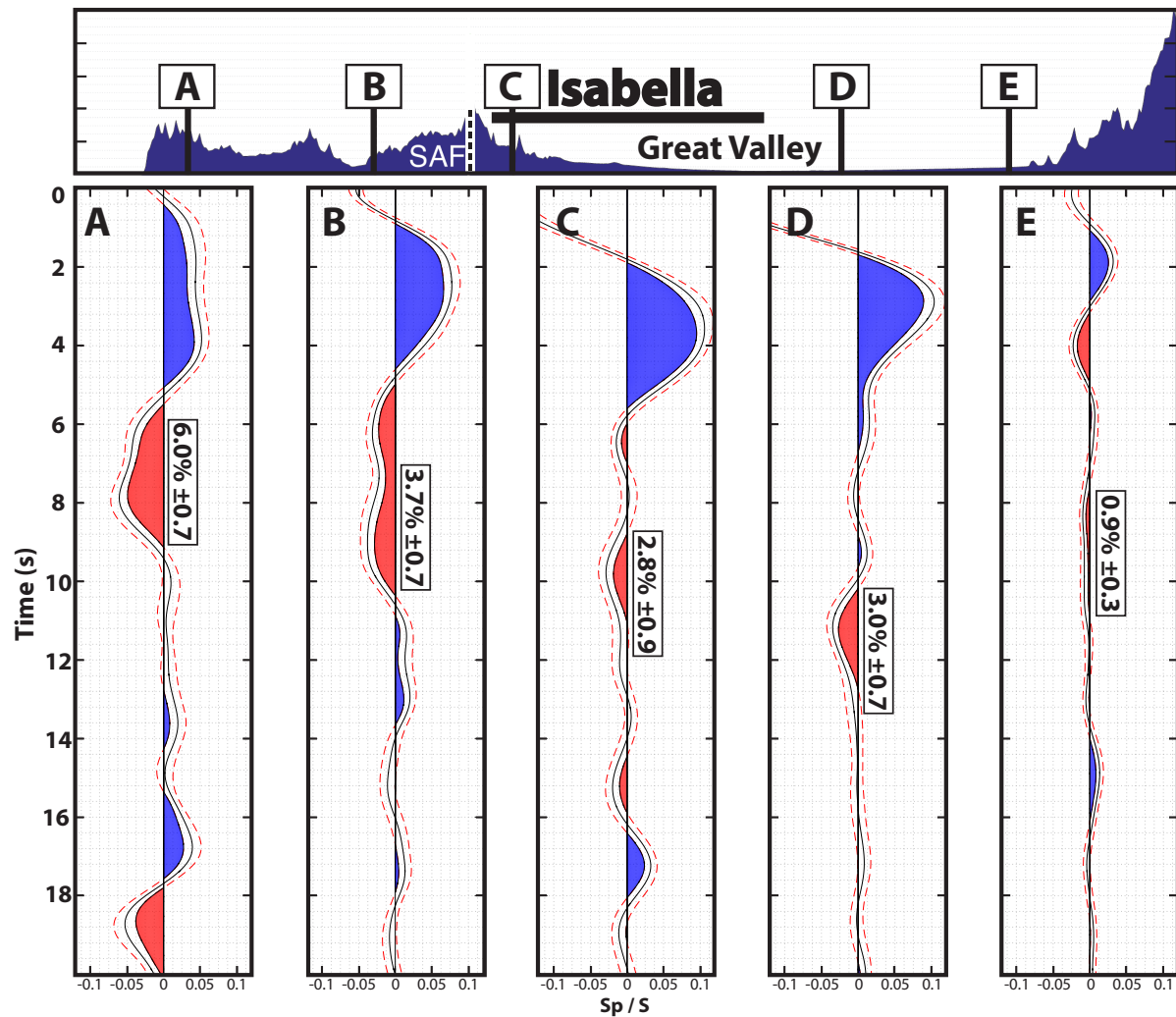


Figure 14. Stacked receiver functions at five points of interest along the CCSE line. Solid black lines are the mean. Dashed red lines are one standard deviation from the mean after randomly resampling the mean at every depth 200 times with replacement. The blue area is the Moho, the red area is the LAB arrival hueristically defined as the first negative arrival shallower than 110km. The stacked spectra on the coast, A, have a peak LAB arrival amplitude of 6.5%. The area immediately to the west of the SAF, B, peaks at 3.4% for the LAB. The area immediately east of the SAF, C, peaks at 2.5% for the LAB. Points D and E in the western and eastern halves of the Great Valley, respectively, show no arrivals with amplitudes consistent with the expected velocity drop at the LAB. The figure at the top is the topographic profile along the CCSE line with the point locations of A,B,C,D,E and the SAF (white line). Black line marks the lateral extent of the Isabella at depths consistent with the LAB from modern S-wave tomography (Schmandt et al., 2015). Dashed lines mark the lateral control for stacking receiver functions at each point of interest.

5.5 Forward modeling

Four possible scenarios for LAB arrivals are evaluated with 1D synthetic seismograms shown in Figure 10. Two are 25km gradients, one with a high shear velocity contrast (10%, blue) and one with a low contrast (5%, red). The other two are over a 10km sharp transition at both a high (10%, black) and low (5%, magenta) contrast. The LAB arrival amplitudes in the sharp transitions range from 3.5-6.0%, the amplitudes for the 25km gradient scenarios range from 2.7-1.8%. The stacked receiver functions at both **A** and **B** are consistent with the synthetic seismograms for a sharp LAB transition between a 5-10% shear velocity contrast. The stack at **C** is comparable with some hybrid between a sharp/low contrast discontinuity and a broad/high contrast discontinuity. The stack at **D** is in agreement with a sharp but very low (<5%) contrast discontinuity. The stacks at **E** are below the arrival amplitudes for even the most subtle LAB scenario (low contrast 25km gradient).

6. Discussion

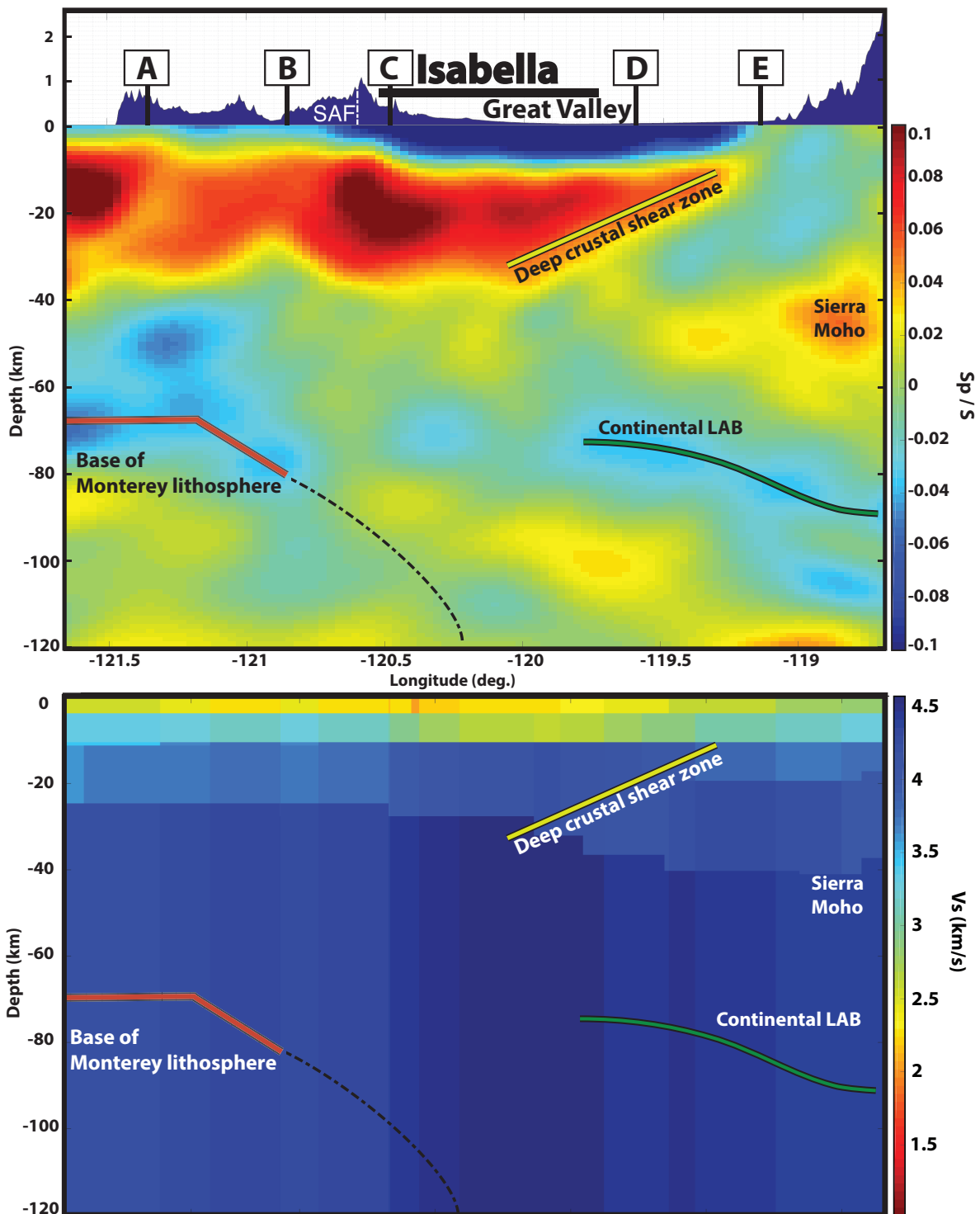


Figure 15. i, the preferred interpretation of CCP image. ii, interpretation overlaid on the shear velocity model (Schmandt et al., 2015) used in CCP imaging. Topographic profile at the top with lateral width of the Isabella at 70km implied in Schmandt et al., 2015. Orange line denotes the interpretation for the negative arrival west of the SAF as conversions at the base of partially subducted Monterey lithosphere. Dashed line denotes the approximate base of a steeply ducting Monterey lithosphere suggested in other studies (e.g. Wang et al., 2013). Green line denotes the interpreted location of a continental LAB. Yellow line denotes a sharp west dipping boundary in conversions at the Moho consistent in dip and depth with a deep crustal shear zone at the base of the metamorphic belt along the Sierra foothills (Miller & Mooney, 1994). At the east end is a positive arrival ~45km in depth interpreted as conversions at a Moho beneath the Sierra Nevada, suggesting the hole observed in the Moho in other studies (e.g. Zandt et al., 2004) to be more localized to the west at these latitudes and not consistent with detachment of overlying mantle lithosphere.

6.1 Coastal block NVG

High amplitude (5-6%) NVG in the uppermost mantle exists from 45-75km in localized areas beneath the coastline up to the SAF (Figure 16), which I interpret to be a conversion caused by either the base of Monterey oceanic lithosphere or a juvenile LAB developed after underplating of the Monterey crust. The arrival is similar in depth but slightly stronger than prior studies on the LAB in central California (Kumar et al., 2012; Ford et al., 2014). The dramatic differences in results between this study and those prior (e.g. Ford et al., 2014) are likely caused by the significant differences in station coverage as well as along-strike heterogeneities in mantle structure at this latitude. Specifically, the Sp results from the CCSE array suggest that the regional scale contrast in Sp converted energy across the San Andreas fault detected by Ford et al. [2014] is locally interrupted at this latitude because of the IA.

The strong NVG beneath the coast may represent the base of Monterey lithosphere. Reflection studies showing the depth of the Monterey crust at the coastal block to be no more than 22km implies these conversions could not be from the top of the oceanic plate. If the NVG represents conversions at the bottom of the Monterey slab then the fossil slab would be between 23-53km thick. The melt-depleted and dehydrated section beneath young oceanic crust near the East Pacific Rise is 50-60km thick (Evans et al., 2005). If a similar lithosphere beneath a partially subducted Monterey crust exists then an NVG between ~70-85km would be expected beneath the coast, which would be consistent with the deeper arrivals for the NVG at the coast. While this cause would be consistent with the deeper arrivals, it does not explain the localized shallow arrival at 45km beneath the coast.

Alternatively, if the Monterey crust was underplated at the margin while the mantle lithosphere of Monterey continued to subduct, the NVG represents a juvenile LAB at the bottom of a thin thermal boundary layer. This would be consistent with conductive cooling models of thermal boundary layer growth (e.g. Parsons & Sclater, 1977; Stein & Stein, 1992) with a depression of the 1200°C isotherm by 20-30km over ~20 myr., predicting an NVG at ~50km. This would be consistent with the shallow arrival at the coast at 45km depth but not consistent with the deeper arrivals at 70-85km depth.

With both of these plausible and mutually exclusive explanations for the coastal NVG, the arrivals cannot constrain the presence or absence of Monterey slab beneath the coastal block. Although we cannot clearly distinguish based on the new Sp CCP imaging alone, the localized absence of coastal block magmatism (Wilson et al., 2005) suggests the complete removal of Monterey mantle lithosphere is unlikely, favoring the NVG occurring across the base of the Monterey lithosphere.

6.2 Absent to weak NVG in the Great Valley

NVG amplitudes east of the SAF are less than half (<1-3%) of those west of the SAF and lie between 1 to 2-sigma bootstrap resampling uncertainty. The NVG arrivals are contained to two areas, a single localized arrival at approximately -120.45 longitude and a mostly coherent and dipping section across the eastern half of the valley. I interpret these arrivals in two scenarios. The first is that the dipping arrivals are conversions at a shallow subducting plate that has retained a basaltic crust yet to transform to eclogite. The second is that the dipping arrivals are conversions at the base of continental lithosphere which is obstructed at the west end of the valley by a steeply dipping oceanic lithosphere.

The first scenario, a shallow dipping plate with basaltic crust, would require the transition of basaltic crust to eclogite to be delayed up to at least 100km depth in order to be consistent with the dipping NVG. However, this would also require the dipping NVG to overly a dipping oceanic Moho (e.g. Li et al., 2003; Peacock, 1993), which is not shown in the CCP image. Furthermore, the transition of basaltic crust to eclogite in a warm subduction zone is expected to happen beginning at about 50-60km depth (Fukao et al., 1983; Peacock, 1993). This would result in diminished to negligible Sp conversions which is also not consistent with the dipping NVG (e.g. Bostock, 2002). Since this dipping horizon exists only below 60km and is also not accompanied with an oceanic Moho, this would not be consistent with either a delayed transition of basalt to eclogite or an eclogitic crust. Consequently, a different explanation appears necessary for the NVG at the eastern end of the CCSE array.

The second scenario, a dipping continental LAB obstructed at the western end of the Great Valley by more steeply dipping oceanic Monterey lithosphere, would require the IA to be constrained to the western half of the Great Valley. Modern tomography (Schmandt et al., 2015; Figure 8) suggests the IA to be more constrained to the western half of the Great Valley than prior studies (Wang et al., 2013) and located over the approximate location of the gap in NVG arrivals at the west end of the valley. This location lacks a coherent horizon of arrivals except for a single highly localized low-amplitude NVG arrival at -120.45 longitude. If Monterey lithosphere begins to have a steeper dip just east of the San Andreas fault, as has been suggested in prior studies (e.g. Wang et al., 2013; Pikser et al., 2012), the slab interfaces could be beyond the theoretical limit for reliable recovery with receiver function CCP imaging (Mackenzie et al, 2010;

Cassidy, 1992). In this context the localized weak NVG arrival beneath the western Great Valley could be an artifact of CCP imaging of a steeply dipping structure.

More generally the obstruction of NVG arrivals at this longitude indicates there is not a sharp sub-horizontal boundary between continental lithosphere and asthenosphere immediately east of the SAF at the latitude of the CCSE array. If the disruption of the NVG arrivals beneath the western Great Valley is caused by a steeply dipping slab, then the re-appearance of NVG arrivals farther east is expected to result from an NVG at the base of North American lithosphere east of the Isabella Anomaly. This would be congruent with the gap in slab-window volcanism (Wang et al., 2013; McLaughlin et al., 1996) at this latitude and the presence of sub-horizontal Monterey microplate oceanic crust beneath coastal California (Meltzer and Levander, 1991).

The preferred interpretation here is that the dipping NVG horizon beneath the eastern half of the valley is more consistent with the base of continental lithosphere. The diminished amplitude for this LAB would be comparable with decreased Sp conversions beneath thick continental lithosphere at 80-100km depth (Abt et al., 2010; Kind et al., 2012), and indicate that there has not been complete removal of mantle lithosphere beneath the Sierra Nevada foothills at this latitude. Such an interpretation would also agree with the Ps conversion arrival at the eastern edge of the CCP image indicating a Moho at the western edge of the Sierra Nevada (Hoots et al., 2015). The presence of thick mantle lithosphere along the western edge of the Sierra Nevada would also be consistent low mantle heat flux in the Sierra Nevada foothills and high mantle heat flux in the high Sierra Nevada (Saltus & Lachenbruch, 1991). Such an interpretation is still consistent with detachment of lower mantle lithosphere to the east of the CCP image

associated with the high elevation area of the southern Sierra Nevada batholith (Liu & Shen, 1998).

6.3 Sierra Nevada foothills Moho

In the CCP image under the Great Valley there is weak or absent Moho conversion and farther east a positive arrival appears at ~45km depth beneath the Sierra foothills. This is consistent with Ps CCP imaging using the CCSE array data (Hoots et al., 2015). The Moho arrival that is shown is somewhat shallower than prior estimates farther to the north in the Sierra foothills (~50-55 km; Frasseto et al., 2011). Prior studies did not clearly image a Moho beneath the foothills and have suggested it was due to partial entrainment of lower crust into a lithospheric drip associated with the Isabella (Zandt et al., 2004). The positive Sp arrival found beneath the Sierra Nevada foothills could make the prior interpretation of a Moho hole locally unnecessary or suggest a smaller area of crustal entrainment away from the latitude of the CCSE array.

6.4 Deep crustal shear zone

Near and above the expected Moho depth beneath the Sierra Nevada foothills, the CCP image shows a sharply west-dipping transition from positive to negative conversions. Preliminary Ps receiver function imaging also highlights this feature (Hoots et al., 2015). This feature is in agreement in dip and depth with a sharp west dipping reflector imaged by Miller et al., 1994 that was interpreted as a deep crustal shear zone along the base of the metamorphic belt along the Sierra Nevada foothills. An alternative interpretation suggests this feature is the top of an accreted ophiolite (Godfrey and Klemperer, 1998). Regardless of interpretation much of this dipping interface may be too shallow to be accurately represented by Sp CCP imaging.

6.5 Conclusion

CCP receiver function imaging of Sp converted waves shows a prominent uppermost mantle NVG west of the SAF, which is interpreted as the base of the partially subducted Monterey microplate. These Sp conversions west of the SAF are in agreement with a sharp LAB contrast, but the wide range in depth of observed NVG arrivals beneath the coastal block suggests greater structural complexity than a single sharp LAB. Whether the mantle section of the lithosphere is composed of Monterey microplate mantle or North America forearc mantle is unknown based on seismic imaging alone, but the absence of post-subduction magmatism on the coastal block favors a Monterey fossil slab origin.

Immediately east of the SAF, a weak-to-absent NVG horizon is interpreted as an area of Monterey whose lithosphere-asthenosphere boundary becomes undetectable as the plate dips too steeply for reliable recovery in CCP imaging. This larger scale gap in a NVG horizon approximately coincides with the width of the IA. Even though CCP imaging showing a local disruption of the LAB cannot constrain the origin of Isabella without also improving the velocity structure model that is used to migrate receiver functions, it does imply that the anomaly is attached or at least adjacent to the overlying North American lithosphere. The results of this study that show a weak-to-absent NVG east of the SAF could be addressed with a more thorough treatment of CCP imaging such as a migration using a 3-D velocity model to accurately constrain the amplitude and polarity of scattered arrivals from steeply dipping interfaces (e.g. Abe et al., 2011; de Kool et al., 2006). Forward modeling to evaluate the accuracy of future scattered wave images could also be improved through use of 2-D or 3-D elastic wave propagation (e.g., Graves, 1996).

If the preferred interpretation in this study is correct and the weak-to-absent NVG is a result of steeply dipping Monterey lithosphere east of the SAF, it would mean this young oceanic lithosphere has undergone >300km of translation with Pacific plate motion beneath North America since 18 Ma without breaking apart (Nicholson et al., 1994; Pikser et al., 2012). One aspect of the CCP imaging that potentially conflicts with the interpretation above is that a localized NVG arrival exists within this gap. This spatially isolated NVG arrival may be an imaging artifact associated with steeply dipping structures.

Sp receiver function CCP imaging results also show a low amplitude NVG dipping to the east in the eastern half of the Great Valley down to about 100km. This would be consistent with conversions at a LAB at the base of continental lithosphere at the western edge of the Sierra Nevada foothills. Sharp changes in arrivals near above the foothills Moho suggest a west dipping crustal interface extending to about 30 km depth. A positive amplitude arrival from Ps conversions at the eastern limit of the CCP detected at 45 km below the Sierra Nevada foothills suggests that, at least at this latitude, the hole in the Moho shown in prior studies of the Sierra Nevada lithosphere is more constrained to the Great Valley. At least at this latitude, this would indicate there is not active entrainment of Sierra Nevada foothills lower crust into the mantle. The results of this study and subsequent interpretations generally in agreement with the tectonic origin theory for the IA (Wang et al., 2013; Pikser et al., 2012) that suggests the anomaly is a continuation of Monterey oceanic lithosphere that begins to dip steeply on the east side of the SAF.

References

- Abe, Y., Ohkura, T., Hirahara, K., & Shibutani, T. (2011). Common-conversion-point stacking of receiver functions for estimating the geometry of dipping interfaces. *Geophysical Journal International*, 185(3), 1305–1311. <http://doi.org/10.1111/j.1365-246X.2011.05001.x>
- Abt, D. L., Fischer, K. M., French, S. W., Ford, H. a., Yuan, H., & Romanowicz, B. (2010). North American lithospheric discontinuity structure imaged by Ps and Sp receiver functions. *Journal of Geophysical Research: Solid Earth*, 115(9), 1–24. <http://doi.org/10.1029/2009JB006914>
- Astiz, L., Earle, P., & Shearer, P. M. (1996). Global Stacking of Broadband Seismograms. *Seismological Research Letters*, 67(4), 8–18. <http://doi.org/10.1785/gssrl.67.4.8>
- Baig, A. M., Bostock, M. G., & Mercier, J. P. (2005). Spectral reconstruction of teleseismic P Green's functions. *Journal of Geophysical Research B: Solid Earth*, 110(8), 1–10. <http://doi.org/10.1029/2005JB003625>
- Bateman, P. C., & Eaton, J. P. (1967). Sierra Nevada Batholith The batholith was generated within a synclinorium. *Science*, 158(3807).
- Becken, M., Ritter, O., Bedrosian, P. a., & Weckmann, U. (2011). Correlation between deep fluids, tremor and creep along the central San Andreas fault. *Nature*, 480(December), 87–90. <http://doi.org/10.1038/nature10609>
- Becker, T. W., Schulte-Pelkum, V., Blackman, D. K., Kellogg, J. B., & O'Connell, R. J. (2006). Mantle flow under the western United States from shear wave splitting. *Earth and Planetary Science Letters*, 247(3-4), 235–251. <http://doi.org/10.1016/j.epsl.2006.05.010>
- Bock, G. (1994). Multiples as precursors to S , SKS and ScS, 421–427.
- Bostock, M. G. (2004). Green's functions, source signatures, and the normalization of teleseismic wave fields. *Journal of Geophysical Research*, 109(B3), 1–15. <http://doi.org/10.1029/2003JB002783>
- Bostock, M. G., Hyndman, R. D., Rondenay, S., & Peacock, S. M. (2002). An inverted continental Moho and serpentinization of the forearc mantle. *Nature*, 417(6888), 536–538. <http://doi.org/10.1038/417536a>
- Boyd, O. S., Jones, C. H., & Sheehan, A. F. (2004). Foundering lithosphere imaged beneath the southern Sierra Nevada, California, USA. *Science (New York, N.Y.)*, 305. <http://doi.org/10.1126/science.1099181>
- Brocher, T. M., Brink, U. S. . T. B., & Abramovitz, T. (1999). Synthesis of Crustal Seismic Structure and Implications for the Concept of a Slab Gap beneath Coastal California. *International Geology Review*, 41(3), 263–274.

- Burdick, L. J., & Langston, C. a. (1977). Modeling crustal structure through the use of converted phases in teleseismic body-wave forms. *Bulletin of the Seismological Society of America*, 67(3), 677–691. Retrieved from <http://www.bssaonline.org/content/67/3/677.abstract>
- Chen, L. (2009). Lithospheric structure variations between the eastern and central North China Craton from S- and P-receiver function migration. *Physics of the Earth and Planetary Interiors*, 173(3-4), 216–227. <http://doi.org/10.1016/j.pepi.2008.11.011>
- Claerbout, J. F., Karrenbach, M., & Balog ..., O. (1992). Earth soundings analysis: processing versus inversion. *Blackwell Scientific Publications, Inc.* Retrieved from <http://en.scientificcommons.org/34783013\npapers://d9fa3861-9e06-4597-b337-32a9e4b37a45/Paper/p172>
- Clark, M. K., Maheo, G., Saleeby, J., & Farley, K. A. (2005). The non-equilibrium landscape of the southern Sierra Nevada, California. *GSA Today*, 15(9).
- de Kool, M., Rawlinson, N., & Sambridge, M. (2006). A practical grid-based method for tracking multiple refraction and reflection phases in three-dimensional heterogeneous media. *Geophysical Journal International*, 167(1), 253–270. <http://doi.org/10.1111/j.1365-246X.2006.03078.x>
- Ducea, M., & Saleeby, J. (1998). A Case for Delamination of the Deep Batholithic Crust beneath the Sierra Nevada, California. *International Geology Review*, 40(1), 78–93. <http://doi.org/10.1080/00206819809465199>
- Dueker, K. G., & Sheehan, A. F. (1998). Mantle discontinuity structure beneath the Colorado Rocky Mountains and High Plains. *Journal of Computational and Applied Mathematics*, 103(B4), 7153–7169.
- Eaton, D. W., Darbyshire, F., Evans, R. L., Grütter, H., Jones, A. G., & Yuan, X. (2009). The elusive lithosphere–asthenosphere boundary (LAB) beneath cratons. *Lithos*, 109(1-2), 1–22. <http://doi.org/10.1016/j.lithos.2008.05.009>
- Escalante, C., Gu, Y. J., & Sacchi, M. (2007). Simultaneous iterative time-domain sparse deconvolution to teleseismic receiver functions. *Geophysical Journal International*, 171(1), 316–325. <http://doi.org/10.1111/j.1365-246X.2007.03511.x>
- Evans, R. L., Hirth, G., Baba, K., Forsyth, D., Chave, A., & Mackie, R. (2005). Geophysical evidence from the MELT area for compositional controls on oceanic plates. *Nature*, 437(7056), 249–252. <http://doi.org/10.1038/nature04014>
- Farra, V., & Vinnik, L. (2000). Upper mantle stratification by P and S receiver functions. *Geophys. J. Int.*, 141, 699–712.
- Ferguson, R. J. (2009). Geophone rotation analysis by polarity inversion. *CREWES Research Report*, 21, 1–12.

- Fischer, K. M., Ford, H. a., Abt, D. L., & Rychert, C. a. (2010). The Lithosphere-Asthenosphere Boundary. *Annual Review of Earth and Planetary Sciences*, 38(1), 551–575.
<http://doi.org/10.1146/annurev-earth-040809-152438>
- Ford, H. A., Fischer, K. M., & Leukic, V. (2014). Localized shear in the deep lithosphere beneath the San Andreas fault system. *Geology*.
- Frassetto, a. M., Zandt, G., Gilbert, H., Owens, T. J., & Jones, C. H. (2011). Structure of the Sierra Nevada from receiver functions and implications for lithospheric foundering. *Geosphere*, 7(4), 898–921. <http://doi.org/10.1130/GES00570.1>
- Fuchs, K., & Mliller, G. (1971). Synthetic Seismograms with the Reflectivity Method and Comparison with Observations. *Geophys. J. Int.*, 23, 417–433.
- Fulton, P. M., & Saffer, D. M. (2009). Potential role of mantle-derived fluids in weakening the San Andreas Fault. *Journal of Geophysical Research: Solid Earth*, 114(April), 1–15.
<http://doi.org/10.1029/2008JB006087>
- Gilbert, H., Jones, C., Owens, T. J., & Zandt, G. (2007). Imaging Sierra Nevada Lithospheric Sinking. *Eos, Transactions American Geophysical Union*, 88(21), 225.
<http://doi.org/10.1029/2007EO210001>
- Godfrey, N. J., Beaudoin, B. C., & Klemperer, S. L. (1997). Ophiolitic basement to the Great Valley forearc basin, California, from seismic and gravity data: Implications for crustal growth at the North American continental margin. *GSA Bulletin*, 108(12), 1536–1562.
- Godfrey, N. J., & Klemperer, L. (1998). Ophiolitic basement to a forearc basin and implications for continental growth : The Coast Range / Great Valley I :: J Sierran basement Franciscan Complex Great Valley, 17(4).
- Gurrola, H., Minster, J. B., & Owens, T. (1994). The Use of Velocity Spectrum For Stacking Receiver Functions and Imaging Upper Mantle Discontinuities. *Geophysical Journal International*, 117(2), 427–440. <http://doi.org/10.1111/j.1365-246X.1994.tb03942.x>
- Hansen, S., & Dueker, K. (2009). P- and S-Wave Receiver Function Images of Crustal Imbrication beneath the Cheyenne Belt in Southeast Wyoming. *Bulletin of the Seismological Society of America*, 99(3), 1953–1961. <http://doi.org/10.1785/0120080168>
- Hansen, S. M., Dueker, K., & Schmandt, B. (2015). Thermal classification of lithospheric discontinuities beneath USArray. *Earth and Planetary Science Letters*, 431, 36–47.
<http://doi.org/10.1016/j.epsl.2015.09.009>
- Henstock, T. J., Levander, A., & Hole, J. A. (2011). Deformation in the Lower Crust of the San Andreas Fault System in Northern California Deformation in the Lower Crust of the San Andreas Fault System in Northern California. *October*, 650(1997).
<http://doi.org/10.1126/science.278.5338.650>

- Houseman, G. A., Neil, E. A., & Kohler, M. (2000). Lithospheric instability beneath the Transverse Ranges of California. *Journal of Geophysical Research*.
- Humphreys, E. D., & Hager, B. (1990). A kinematic model for the late Cenozoic development of southern California crust and upper mantle. *Journal of Geophysical Research-Solid Earth*, 95(B12), 19747. <http://doi.org/10.1029/JB095iB12p19747>
- Jones, C. H., Kanamori, H., & Roecker, S. W. (1994). Missing roots and mantle “drips”: Regional Pn and teleseismic arrival times in the southern Sierra Nevada and vicinity, California. *Journal of Geophysical Research*, 99(03), 4567–4601.
- Jones, C. H., Reeg, H., Zandt, G., Gilbert, H., Owens, T. J., & Stachnik, J. (2014). P-wave tomography of potential convective downwellings and their source regions, Sierra Nevada, California. *Geosphere*, 10(3), 505–533. <http://doi.org/10.1130/GES00961.1>
- Kennett, B. L. N., & Engdahl, E. R. (1991). Traveltimes for global earthquake location and phase identification, 429–465.
- Kind, R., Yuan, X., & Kumar, P. (2012). Seismic receiver functions and the lithosphere–asthenosphere boundary. *Tectonophysics*, 536–537, 25–43. <http://doi.org/10.1016/j.tecto.2012.03.005>
- Kind, R., Yuan, X., Mechie, J., & Sodoudi, F. (2015). Structure of the upper mantle in the north-western and central United States from USArray S-receiver functions. *Solid Earth Discussions*, 7(1), 1025–1057. <http://doi.org/10.5194/sed-7-1025-2015>
- Kumar, P., Kind, R., Yuan, X., & Mechie, J. (2012). USArray Receiver Function Images of the Lithosphere-Asthenosphere Boundary. *Seismological Research Letters*, 83(3), 486–491. <http://doi.org/10.1785/gssrl.83.3.486>
- Langston, C. A. (1979). Structure Under Mount Ranier, Washington, Inferred From Teleseismic Body Waves, 84(9).
- Lekić, V., & Fischer, K. M. (2013). Contrasting lithospheric signatures across the western United States revealed by Sp receiver functions. *Earth and Planetary Science Letters*, 1, 1–9. <http://doi.org/10.1016/j.epsl.2013.11.026>
- Lekic, V., French, S. W., & Fischer, K. M. (2011). Lithospheric Thinning Beneath Rifted Regions of Southern California. *Science* .
- Levander, A., & Miller, M. S. (2012). Evolutionary aspects of lithosphere discontinuity structure in the Western U.S. *Geochemistry, Geophysics, Geosystems*, 13(1), 1–22. <http://doi.org/10.1029/2012GC004056>

- Li, X., Yuan, X., & Kind, R. (2007). The lithosphere-asthenosphere boundary beneath the western United States. *Geophysical Journal International*, 170(2), 700–710. <http://doi.org/10.1111/j.1365-246X.2007.03428.x>
- Liu, M., & Shen, Y. (1998). Sierra Nevada uplift: A ductile link to mantle upwelling under the Basin and Range province. *Geology*, 26(4), 299–302. [http://doi.org/10.1130/0091-7613\(1998\)026<0299:SNUADL>2.3.CO;2](http://doi.org/10.1130/0091-7613(1998)026<0299:SNUADL>2.3.CO;2)
- Lonsdale, P. (1991). Structural patterns of the Pacific floor offshore of peninsular California. *The Gulf and Peninsular Province of the Californias*, 47, 87–125. Retrieved from http://scholar.google.com/scholar?q=related:Ob4rC3E0FgsJ:scholar.google.com/&hl=en&num=30&as_sdt=0,5
- Meltzer, A. S., & Levander, A. R. (1991). Deep crustal reflection profiling offshore southern central California. *Journal of Geophysical Research*, 96(B4), 6475. <http://doi.org/10.1029/91JB00120>
- Mercier, J., Bostock, M. G., & Baig, A. M. (2006). Improved Green ' s functions for passive-source structural studies. *Geophysics*, 71(4).
- Miller, K. C., Howie, J. M., & Stanley, R. D. (1992). Shortening within unthinned oceanic crust beneath the Central California Margin. *Journal of Geophysical Research*, 97(B13200009, jv,), 19,919–961,980.
- Miller, K. C., & Mooney, W. D. (1994). Crustal structure and composition of the southern Foothills Metamorphic Belt, Sierra Nevada, California, from seismic data, 99(93), 6865–6880.
- Nicholson, C., Sorlien, C. C., Atwater, T., Crowell, J. C., & Luyendyk, B. P. (1994). Microplate capture, rotation of the western Transverse Ranges, and initiation of the San Andreas transform as a low-angle fault system. *Geology*, 22(6), 491–5.
- Nicholson, C., Sorlien, C. C., & Luyendyk, B. P. (1992). Deep crustal structure and tectonics in the offshore southern Santa Maria Basin, California. *Geology*, 20(3), 239–242.
- Park, S. K. (2004). Mantle heterogeneity beneath eastern California from magnetotelluric measurements. *Journal of Geophysical Research B: Solid Earth*, 109, 1–13. <http://doi.org/10.1029/2003JB002948>
- Parsons, B., & Sclater, J. G. (1977). An Analysis of the Variation of Ocean Floor Bathymetry and Heat Flow with Age. *Journal of Geophysical Research*, 82(6).
- Phinney, R. A. (1964). Structure of the Earth's crust from spectral behavior of long-period body waves. *Journal of Geophysical Research*, 69(14), 2997–3017. <http://doi.org/10.1029/JZ069i014p02997>

- Pikser, J. E., Forsyth, D. W., & Hirth, G. (2012). Along-strike translation of a fossil slab. *Earth and Planetary Science Letters*, 331-332, 315–321. <http://doi.org/10.1016/j.epsl.2012.03.027>
- Pourhiet, L. Le, Gurnis, M., & Saleeby, J. (2006). Mantle instability beneath the Sierra Nevada Mountains in California and Death Valley extension. *Earth and Planetary Science Letters*, 251(1-2), 104–119. <http://doi.org/10.1016/j.epsl.2006.08.028>
- Raikes, S. (1976). The azimuthal variation of teleseismic P-wave residuals for stations in southern California. *Earth and Planetary Science Letters*, 29.(2), 367–372.
- Rondenay, S., Bostock, M. G., & Shragge, J. (2001). Multiparameter two-dimensional inversion of scattered teleseismic body waves 3 . Application to the Cascadia 1993 data set, 106(12), 30795–30807.
- Russell, P. C., Mclaughlin, R. J., Sliter, W. V, & Sorg, D. H. (1996). Large-scale displacement on the East San Francisco Bay Region fault system , California : Implications for location of late Miocene to Pliocene Pacific plate boundary older •• Jurassic, 15(1), 1–18.
- Rychert, C. A., Fischer, K. M., & Rondenay, S. (2005). A sharp lithosphere-asthenosphere boundary imaged beneath eastern North America. *Nature*, 436(7050), 542–545. <http://doi.org/10.1038/nature03904>
- Rychert, C. a., Shearer, P. M., & Fischer, K. M. (2010). Scattered wave imaging of the lithosphere-asthenosphere boundary. *Lithos*, 120(1-2), 173–185. <http://doi.org/10.1016/j.lithos.2009.12.006>
- Saleeby, J. (2003). Segmentation of the Laramide Slab—evidence from the southern Sierra Nevada region. *Geological Society of America Bulletin*, 115(6), 655–668. [http://doi.org/10.1130/0016-7606\(2003\)115<0655:SOTLSF>2.0.CO;2](http://doi.org/10.1130/0016-7606(2003)115<0655:SOTLSF>2.0.CO;2)
- Saleeby, J., & Foster, Z. (2004). Topographic response to mantle lithosphere removal in the southern Sierra Nevada region, California . *Geological Society of America*.
- Savage, B., & Silver, P. G. (2008). Evidence for a compositional boundary within the lithospheric mantle beneath the Kalahari craton from S receiver functions. *Earth and Planetary Science Letters*, 272(3-4), 600–609. <http://doi.org/10.1016/j.epsl.2008.05.026>
- Schmandt, B., & Humphreys, E. (2010a). Complex subduction and small-scale convection revealed by body-wave tomography of the western United States upper mantle. *Earth and Planetary Science Letters*, 297(3-4), 435–445. <http://doi.org/10.1016/j.epsl.2010.06.047>
- Schmandt, B., & Humphreys, E. (2010b). Seismic heterogeneity and small-scale convection in the southern California upper mantle. *Geochemistry, Geophysics, Geosystems*, 11(5), 1–19. <http://doi.org/10.1029/2010GC003042>

- Schweickert, R. a., & Cowan, D. S. (1975). Early Mesozoic tectonic evolution of the western Sierra Nevada, California. *Geological Society of America Bulletin*, 86(10), 1329. [http://doi.org/10.1130/0016-7606\(1975\)86<1329:EMTEOT>2.0.CO;2](http://doi.org/10.1130/0016-7606(1975)86<1329:EMTEOT>2.0.CO;2)
- Silver, P. G., & Holt, W. E. (2002). The mantle flow field beneath western North America. *Science (New York, N.Y.)*, 295(2001), 1054–1057. <http://doi.org/10.1126/science.1066878>
- Stein, C. A., & Stein, S. (1992). A model for the global variation in oceanic depth and heat flow with lithospheric age. *Nature*, 359(9), 123–129.
- Van Wijk, J. W., Govers, R., & Furlong, K. P. (2001). Three-dimensional thermal modeling of the California upper mantle: A slab window vs. stalled slab. *Earth and Planetary Science Letters*, 186, 175–186. [http://doi.org/10.1016/S0012-821X\(01\)00243-6](http://doi.org/10.1016/S0012-821X(01)00243-6)
- VanDecar, J., & Crosson, R. (1990). Determination of teleseismic relative phase arrival times using multi-channel cross-correlation and least squares. *Bulletin of the Seismological Society of America*, 80(1), 150–169. Retrieved from <http://www.bssaonline.org/content/80/1/150.short>
- Vinnik, L., Kurnik, E., & Farra, V. (2005). Lehmann discontinuity beneath North America: No role for seismic anisotropy. *Geophysical Research Letters*, 32(9), 1–4. <http://doi.org/10.1029/2004GL022333>
- Vinnik, L. P. (1977). Detection of waves converted from P to SV in the mantle. *Physics of the Earth and Planetary Interiors*, 15(1).
- Wang, Y., Forsyth, D. W., Rau, C. J., Carriero, N., Schmandt, B., Gaherty, J. B., & Savage, B. (2013). Fossil slabs attached to unsubducted fragments of the Farallon plate. *Proceedings of the National Academy of Sciences of the United States of America*, 5342–6. <http://doi.org/10.1073/pnas.1214880110>
- Wilson, D. C., Angus, D. a., Ni, J. F., & Grand, S. P. (2006). Constraints on the interpretation of S-to-P receiver functions. *Geophysical Journal International*, 165(3), 969–980. <http://doi.org/10.1111/j.1365-246X.2006.02981.x>
- Yan, Z., & Clayton, R. W. (2007). A notch structure on the Moho beneath the Eastern San Gabriel Mountains. *Earth and Planetary Science Letters*, 260(3-4), 570–581. <http://doi.org/10.1016/j.epsl.2007.06.017>
- Yan, Z., & Clayton, R. W. (2007). Regional mapping of the crustal structure in southern California from receiver functions. *Journal of Geophysical Research: Solid Earth*, 112(5), 1–20. <http://doi.org/10.1029/2006JB004622>
- Yuan, X., Kind, R., Li, X., & Wang, R. (2006). The S receiver functions: synthetics and data example. *Geophysical Journal International*, 165(2), 555–564. <http://doi.org/10.1111/j.1365-246X.2006.02885.x>

- Zandt, G. (2003). The Southern Sierra Nevada Drip and the Mantle Wind Direction Beneath the Southwestern United States. *International Geology Review*, 45, 213–224.
<http://doi.org/10.2747/0020-6814.45.3.213>
- Zandt, G., Gilbert, H., Owens, T. J., Ducea, M., Saleeby, J., & Jones, C. H. (2004). Active foundering of a continental arc root beneath the southern Sierra Nevada in California. *Nature*, 431(9), 41–6. <http://doi.org/10.1038/nature02847>
- Zhu, L., & Kanamori, H. (2000). Moho depth variation in southern California, 105, 2969–2980.